JBC Papers in Press. Published on November 3, 2016 as Manuscript M116.747089
The latest version is at http://www.jbc.org/cgi/doi/10.1074/jbc.M116.747089

Oxidative Unfolding of the Rubredoxin Domain and the Natively Disordered N-terminal Region Regulate the Catalytic Activity of *M. tuberculosis* Protein Kinase G

Matthias Wittwer[1a], Qi Luo[1b,2], Ville R. I. Kaila [1b], and Sonja A. Dames[1a,3§]

[1a/b]Technische Universität München, Department of Chemistry, [a]Biomolecular NMR Spectroscopy/[b]Computational Biocatalysis, Lichtenbergstr. 4, 85747 Garching, Germany
[2]Soft Matter Research Center and Department of Chemistry, Zhejiang University, 310027, P.R. China
[3]Institute of Structural Biology, Helmholtz Zentrum München, Ingolstädter Landstr. 1, 85764 Neuherberg, Germany

[§]To whom correspondence may be addressed. E-mail: sonja.dames@tum.de

Running title

Regulation of mycobacterial protein kinase G by redox changes and disordered regions

Key words

Mycobacterium tuberculosis protein kinase G, redox-sensitive metal binding motif, rubredoxin, oxidative unfolding, MD simulations, NMR spectroscopy, kinase assay.

Abstract

Mycobacterium tuberculosis escapes killing in human macrophages by secreting protein kinase G (PknG). PknG intercepts host signaling to prevent the fusion of the phagosome engulfing the mycobacteria with the lysosome and thus their degradation. The N-terminal NORS (no regulatory secondary structure) region of PknG (residues ~1-75) has been shown to play a role for PknG regulation by (auto-) phosphorylation, whereas the following rubredoxin-like metal-binding motif (RD, residues ~74–147) has been shown to interact tightly with the subsequent catalytic domain (residues ~148–420) to mediate its redox regulation. Deletions or mutations in the NORS or the redox-sensitive RD significantly decrease PknG survival function. Based on combined nuclear magnetic resonance (NMR) spectroscopy, *in vitro* kinase assay, and molecular dynamics (MD) simulation data we provide novel insights in the regulatory roles of the N-terminal regions. The NORS region is indeed natively disordered and rather dynamic. Consistent with most earlier data, autophosphorylation occurs also in our assays only if the NORS region is present and thus in the NORS region. Phosphorylation of it results only in local conformational changes and does not induce interactions with the subsequent RD. Although the reduced, metal bound RD makes in the published crystal structures tight interactions with the following catalytic domain, it can also fold in its absence. Our data further suggest that oxidation-induced unfolding of the RD regulates substrate access to the catalytic domain and thereby PknG function under different redox conditions, e.g. if exposed to increased levels of reactive oxidative species (ROS) in host macrophages.

Introduction

Mycobacterium tuberculosis (Mtb), the causative agent of tuberculosis, has evolved different mechanisms to monitor redox signals. The capability of Mtb to sense redox stress and to maintain redox homeostasis is important for the survival of the pathogen in the human host (1-3). Recent studies have shown that redox stress responses of mycobacteria are linked to the phosphorylation of several proteins by eukaryotic-like serine/threonine kinases (eSTKs) (4,5). Of the eleven eSTKs encoded by the Mtb genome (6), protein kinase G (PknG) and E (PknE) harbor specific redox-sensitive motifs

(7,8). The soluble protein kinase G (PknG) has been proposed to promote cellular survival of mycobacteria in host macrophages by blocking their lysosomal delivery and thus degradation (9). Moreover, since PknG is secreted into the cytosol of host macrophages, it is a promising drug target (9). PknG is a multidomain protein consisting of four functional regions (Fig. 1A). The N-terminal ~75 residues of the no regulatory secondary structure (NORS)[†] region have been suggested to be intrinsically disordered and to harbor a major *in vivo* phosphorylation site at threonine (T63) (8,10,11). Based on the crystal structure of an N-terminal truncated variant (PknG74-750) in complex with a newly detected inhibitor (AX20017, Fig. 1B), the following redox-sensitive rubredoxin-like metal binding domain (RD) makes tight interactions with the catalytic domain (8). C-terminally the kinase domain is flanked by a tetratricopeptide repeat domain (TPRD), a structural motif typically involved in protein-protein interactions (8).

PknG can autophosphorylate itself in trans (11). However, in contrast to other (mycobacterial) kinases, the autophosphorylation does not affect the kinase activity, but is required for the survival of pathogenic mycobacteria within host macrophages (10). In rubredoxins an iron atom is typically tetrahedrally coordinated by four cysteine residues (12), but other metal ions such cobalt, nickel, and zinc can replace the iron (13). The redox-sensitive RD of PknG contains two C-X-X-C-G motifs (Fig. 1A) that can *in vitro* coordinate a divalent metal ion, such as zinc, iron, or cadmium in the reduced state (8,14-16). However, it is currently unknown, which metal ion is coordinated under *in vivo* conditions. Three crystal structures of PknG have been published, one of PknG74-750 (RD-KD-TPRD) with the RD coordinating Cd^{2+} and the KD in complex with the small molecule inhibitor AX20017 (PDB-ID 2PZI, Fig. 1B) and two of PknG74-405 (RD-KD) with the RD coordinating Zn^{2+} and the KD in complex with either an ATP analogue (ATP-γS) or ADP as well as Mg^{2+} (PDB-IDs 4Y12 and 4Y0X) (8,14). The structure of the RD is very similar in all three solved structures, but the orientation of the RD with respect to the kinase domain is slightly different. In the inhibitor bound structure, the RD interacts with the N-terminal and C-terminal lobes of the kinase domain, whereas in the ATP analogue bound form, the RD makes contacts only with the N-terminal lobe (8,14). It was proposed that the RD regulates the intrinsic kinase activity by restricting the accessibility of the active site (8,14). Mutation of all four cysteines in the two conserved C-X-X-C-G motifs to alanines or serines impair the kinase activity and render PknG insensitive to a regulation by redox changes (8,11).

Cells of the innate immune system such as macrophages release high concentrations of reactive oxidative species (ROS) to kill engulfed pathogenic bacteria (17). However, based on the published crystal structures and functional data for wild type and mutant PknG proteins, the exact mechanism of the redox regulation of the kinase activity under oxidative stress conditions remains elusive. Here, we present combined nuclear magnetic resonance (NMR) spectroscopy, *in vitro* kinase assay, and molecular dynamics (MD) simulations data that show how the dynamics as well as the local and global structure of PknG change upon oxidation of the RD and that the so far uncharacterized NORS region is indeed natively unfolded and the target region for PknG autophosphorylation in trans.

Results

The NORS region shows only local structural order and the RD can fold in the absence of the KD

The structural properties and dynamics of the N-terminal NORS region and of the RD in the absence of the kinase domain have not been described yet. The ^{1}H-^{15}N-HSQC spectrum of the two segment protein His-PknG1-147 (NORS-RD, SI Fig. S1) represents almost perfectly the sum of those of each isolated functional region (His-PknG1-75 & PknG74-147, SI Fig. S1). This indicates that the NORS

[†] NORS, no regulatory secondary structure, in case of PknG corresponding to the natively disordered region (residues 1 to ~75); PknG, protein kinase G, (His-)PknG1-75/1-147, (MGSSHHHHHHSSGLVPRGSH- followed by) residues 1-75/1-147 of *mycobacterium tuberculosis* PknG; PknG74-147, residues 74-147 of *mycobacterium tuberculosis* PknG; RD, rubredoxin-like domain, in case of PknG corresponding to residues 74-147; SI, supplementary information; TCEP, tris(2-carboxyethyl)phosphin.

region and the RD behave rather independently and do not significantly interact. The low signal dispersion of the NORS region indicates already that is indeed a natively disordered protein (IDP) region. To determine in more detail the secondary structure content of each region we measured $^{13}C^{\alpha}$ secondary shifts (Fig. 1C) and for PknG74-147 further $^{3}J_{HNH\alpha}$ scalar couplings (SI Fig. S2A) and $^{1}H^{\alpha}$ secondary shifts (SI Fig. S2B). To characterize the backbone dynamics of the two segment protein His-PknG1-147 (NORS-RD) and of each isolated functional region (His-PknG1-75 & PknG74-147) we recorded ^{15}N-relaxation data including $\{^{1}H\}$-^{15}N-NOE (Fig. 1D) as well as ^{15}N-T_1, and -T_2 data (SI Fig. S3A & SI results). In addition, we back calculated the $^{13}C^{\alpha}$ secondary shifts from the available crystal structures of PknG using the program Sparta+ (18) and compared them to the experimentally determined ones (SI Fig. S4).

The NORS region (residues ~1-75) shows strongly negative $^{13}C^{\alpha}$ secondary shifts for residues preceding a proline. However, the majority of the remaining residues show only a weak propensity for α-helical secondary structure (Fig. 1C, blue bars). The $^{3}J_{HNH\alpha}$ scalar couplings for the NORS region (SI Fig. S2A, blue data) are mostly between 6-8 Hz, indicating that it does not stably populate α-helical or β-sheet secondary structure and may overall only transiently and locally populate more ordered states. This is consistent with $\{^{1}H\}$-^{15}N-NOE values typical for dynamic regions, with negative values below -0.2 for the isolated NORS region (Fig. 1D, blue symbols) and values between about 0.2 and -0.4 if connected to the RD (Fig. 1D, black symbols). The region between residues 20 and 40 appears overall more dynamic in His-PknG1-75 compared His-PknG1-147, which is also reflected in the ^{15}N-T_1, and -T_2 data (SI Fig. S3A & SI results). This suggests that the presence of the RD influences the dynamics of this central region of the NORS. Overall, the NORS region appears as predicted natively disordered. However it may transiently populate α-helical stretches that are interrupted by several prolines (10) that may induce local backbone kinks or turns (19).

The RD shows, consistent with the large chemical shift dispersion for the residues around the two C-X-X-C-G metal coordinating motifs (^{106}C-W-N-C-G^{110} & ^{128}C-P-Y-C-G^{132}), larger positive and negative $^{13}C^{\alpha}$ secondary shifts than the NORS region (Fig. 1C, red bars). Thus it appears to be present in a folded metal bound state. Since the RD interacts tightly with the KD in the crystal structure of PknG74-750 bound to an inhibitor (PDB-ID 2PZI, Fig. 1B), its presence might be needed to stabilize the folded state of the RD. However, the α-helix (~89-92), the 3^{10} helix (~101-103), and the two β-strands (~125-127 & ~134-136) detected in the crystal structure (schematically indicated at the top) appear to be similarly present in the solution state of the RD not connected to the kinase. Metal coordination to the cysteines in the two C-X-X-C-G motifs (~106-110 and ~128-132) induces the formation of turns, which as helical regions show rather strong positive $^{13}C^{\alpha}$ secondary shifts (Fig. 1C). The RD has as many prolines as the NORS region (each 10). Besides being involved in the already mentioned helical, sheet, and turn regions, they are further present in turns or β-bridges. The region including the 3^{10} helix and the following C-X-X-C-G motifs (~100-140) shows in the isolated RD and connected to the NORS region $\{^{1}H\}$-^{15}N-NOE values ~0.4-0.8 (Fig. 1D), which are typical for rather well structured regions. However, NOE values ~0-0.2 indicate that the N-terminal α-helical stretch is already more dynamic and negative values for the N- and C-terminal ends of the isolated RD indicate even further increased backbone dynamics on the ns-ps time scale. Since the $^{13}C^{\alpha}$ secondary shifts and the $\{^{1}H\}$-^{15}N-NOE values for the reduced, metal bound RD are almost the same for His-PknG1-147 and PknG74-147, the presence of the NORS regions has no significant influence on its structure as well as backbone dynamics. This can be explained by the NORS being natively disordered as well as connected to the RD by a dynamic linker region rich in glycines (G76-G78).

The fold of the isolated reduced metal bound RD in solution is overall similar to the one attached to the kinase in complex with AX20017 or ADP or ATP-γS in the crystal state

Since the RD interacts tightly with the kinase domain in the available three crystal structures, albeit to a slightly different extent (8,14), we further analyzed the effect of the presence of the kinase domain on the structure of the reduced, metal bound state. Based on the superposition of the ^{1}H-^{15}N-HSQC spectra of His-PknG74-420 encompassing the RD and the kinase and the RD-only protein PknG74-147 (SI

Fig. S5), peaks for several residues are found at similar chemical shift values, e.g. those for the two side chain amide protons of W107 and W127 of the RD. However, overall these data do not allow us to determine in detail how similar the conformations of the RD in both proteins are. We thus recorded backbone ^{15}N-^{1}H RDCs to compare the conformation of the RD in the isolated state to that in the available crystal structure data. Fig. 1E shows a plot of the experimentally obtained RDCs as function of the residue sequence position compared to those back calculated from the crystal structures of His-PknG74-750 (RD-KD-TPRD) in complex with a small molecule inhibitor (PDB-ID 2PZI, Fig. 1B & SI Fig. S6A) and of PknG74-405 (RD-KD) in complex with either ADP (PDB-ID 4Y0X, SI Fig. S6A) or an ATP analogue (PDB-ID 4Y12, SI Fig. S6A). The respective plots of the experimental versus calculated values for each crystal structure and a larger representation of the RD structure are shown in SI Fig. S6B. Overall the conformation of the isolated RD in solution is, as already indicated by the comparison of the experimental and back calculated chemical shift data (SI Fig. S4) very similar to that in the presence of the kinase in the three crystal structures. The observed differences around the C-X-X-C-G motifs (residues 106-110 & 128-132) and near residue 115 between the experimental RDCs and those back calculated based on the crystal structures can be accounted for by missing contacts to the kinase domain in the isolated RD and slightly different contacts in PDB-ID 2PZI versus 4Y0X and 4Y12, as well as by the fact that the RD has regions with increased backbone dynamics in solution (Fig. 1D) and in the crystal states, e.g. no coordinates for residues 116-121 in PDB-ID 2PZI and higher B-factors in the RDs of all crystal structures (SI Fig. S6A).

Deletion of the NORS and TPRD, different redox conditions, and the folding state of the substrate influence the catalytic efficiency of PknG

In order to better understand the relevance of the redox-sensitive RD as well as of the NORS region for the regulation of PknG function and to complement and resolve partially contradictory results from the literature (8,10,11,14), we first also performed *in vitro* kinase assays monitoring the progress of substrate phosphorylation based on the use of radio labeled ATP. Since PknG can autophosphorylate itself in trans in the NORS region (10), we used as substrate His-PknG1-147 encompassing both the NORS and the RD (Fig. 2A, SI Fig. S7A-C). Fig. 2A shows the phosphorimager kinase activity data using as kinases either His-tagged full length wild type (wt) PknG, or the NORS deletion mutant His-Pkng74-750, or the NORS and TPRD deletion mutant His-PknG74-420, all with the RD in the folded, Zn bound state, and as substrate His-PknG1-147 with the RD either in the reduced, Zn bound or the oxidized state. Note, that a fraction of the usually higher activity of the wild type protein arises from the additional phosphorylation of its own NORS region (SI Fig. S7A and C). Compared to the wild type (Fig. 2A, blue bars), deletion of the N-terminal NORS region reduces PknG catalytic activity significantly (Fig. 2A, green bars) and additional removal of the C-terminal TPRD results in a further reduction (Fig. 2A, red bars). This is consistent with published results (10,11,14). Oxidized His-PknG1-147 is overall a better substrate than the protein with the RD in the reduced, metal bound state (Fig. 2A, left versus right bar of each set of differently colored bars). This suggests that PknG autophosphorylation is more efficient if the RD of the substrate is in the oxidized state, which may facilitate binding to the catalytic cleft, especially for the phosphorylation of T63 and T64, which are close to the N-terminal end of the RD around residue 74. SI Fig. S7B shows phosphorimager kinase activity data from assays using as kinase either the full length wild type protein His-PknG1-750 or the NORS deletion mutant His-PknG74-750 with the RD either in the reduced, Zn bound or the oxidized state and as substrate again His-PknG1-147 with the RD also either coordinating Zn^{2+} or being oxidized. The corresponding SDS PAGE analysis is shown in SI Fig. S7C. The kinase with the RD in the metal bound state phosphorylates the substrate with the RD in the oxidized state a bit better. If the RD of the kinase is in the oxidized state, the folding state of the RD in the substrate appears not to have a significant influence on the catalytic efficiency.

PknG autophosphorylation induces only local conformational changes but no global folding of the NORS region

Complementary to the phosphorimager kinase activity data, we monitored the phosphorylation of the NORS-RD protein His-PknG1-147 (Fig. 2B) or the NORS-only protein

His-PknG1-75 (SI Fig. S7D) based on spectral changes in ^{1}H-^{15}N-HSQC spectra. Phosphorylation of both substrates in ^{15}N-labeled form by unlabeled His-PknG74-420 (RD-KD) results in the shift or disappearance and reappearance at new positions of several peaks of the NORS region. Based on the available assignments this includes residues near the known *in vivo* phosphorylation site T63 (11) as well as residues near other threonine residues know to be phosphorylated *in vitro* (T23, T32, T64) (10). Overall, His-PknG1-147 is more efficiently phosphorylated than His-PknG1-75. The appearance of some new more well dispersed peaks, e.g. around 8.7-9.3 ppm in the ^{1}H dimension (Fig. 2B, SI Fig. S7D) suggests that autophosphorylation induces locally more ordered states, but not a global folding of the NORS region.

The PknG RD can switch between a reduced, metal bound folded and an oxidized, metal free unfolded state

Since replacement of the cysteines of the rubredoxin-like RD to alanines or serines disables the redox regulation of PknG kinase function and based on fluorescence data results in significant structural changes (8,11), we also recorded ^{1}H-^{15}N-HSQC data of His-PknG1-147 (NORS-RD) under different redox conditions (Fig. 3A). If $ZnCl_2$ is added upon induction of the expression of His-PknG1-147 the black spectrum is obtained (15). This contains a subspectrum with mostly well dispersed peaks that is largely identical to the spectrum of the isolated RD (PknG74-147) that is obtained if the RP-HPLC purified protein is refolded by adding a reducing agent such as TCEP and a divalent metal ion such Zn^{2+} (SI Fig. S8A) (15). As other rubredoxin motifs, the RD can also coordinate other metal ions such Cd^{2+} as in the crystal structure of PknG74-750 in complex with AX20017 (8), or Mn^{2+}, Co^{2+}, or Fe^{3+} as indicated by the ^{1}H-^{15}N-HSQC data of His-PknG1-147 shown in SI Fig. S9. Due to the paramagnetic nature of the used metal ions, the well-dispersed NMR signals of the RD are mostly not visible. However the overall change of the spectral appearance indicates a structural transition upon metal addition (SI Fig. S9, see also SI results). Expression of PknG1-147 in minimal medium without addition of $ZnCl_2$ upon induction or addition of a rather mild oxidizing agent such as H_2O_2 together with a metal chelator such as EDTA results in the red spectrum that shows a low dispersion for all signals. Again the spectrum of the oxidized, metal free isolated RD (PknG74-147, SI Fig. S8A, see also the $\{^{1}$H$\}$-^{15}N-NOE data in SI Fig. S3B) represents a subspectrum of that of oxidized His-PknG1-147 (SI Fig. S8B). Indicated by the low signal dispersion, the RD in the oxidized, metal free form is as the NORS largely unfolded. The spectrum of a mutant of His-PknG1-147 in which all four cysteines of the two C-X-X-C-G motifs have been replaced by serines (His-PknG1-147-4C/S) looks overall similar to that of the oxidized, metal free state (SI Fig. S8C). Altogether, the data indicate that the RD can switch between a reduced, metal bound folded state and an oxidized, metal free unfolded state (Fig. 3B). Thus a change of the redox conditions may regulate the catalytic kinase domain by controlled un- and refolding of the RD, which is expected to influence the substrate access.

MD simulations indicate that oxidation of the RD increases the accessibility of ATP in the substrate binding region

The available crystal structures for PknG fragments containing both the RD and the kinase domain do not explain how oxidation of the two C-X-X-C-G motifs in the RD affects the conformation and accessibility of the catalytic domain and thus its activity. To complement the above structural and dynamic NMR data for the RD in different redox states, we performed six independent 250 ns MD simulations of PknG74-420 (RD-KD) with the C-X-X-C-G motifs of the RD either coordinating a metal ion (Fe^{2+}) or with a disulfide bond in each motif (C106-C109 & C128-C131) (SI Fig. S10A). Our simulations indicate that oxidization of the RD leads, on average, to a more open and better accessible ATP substrate-binding cavity (Fig. 3C). In line with the NMR data of the RD under different redox conditions (Fig. 3A, SI Fig. S8A, B), we find that the RD containing the two C-X-X-C-G motifs shows overall an increased likelihood to unfold in the oxidized metal free form, which may also favor the substrate access due to reduced steric clashes between the RD and the ATP binding site. In order to quantify the structural changes within the substrate-binding pocket, we calculated the average extension of three loops surrounding the ATP site ($\langle d_{Loop} \rangle$, Fig. 3D-F & SI Fig. S10B), as well as the ATP cavity volume, and solvent accessible surface area (SASA) of residues interacting with ATP, as suggested by Scherr *et al*. (8). The

simulations suggest that loops 1 and 3 surrounding the ATP-binding site become more extended in the oxidized states (Fig. 3E, F), making the cavity more accessible from the bulk. Oxidization of the RD also seems to lead to a somewhat larger cavity volume and SASA of ATP-surrounding residues (SI Table 1, Fig. S11). In addition to these differences in substrate accessibility, our simulations further suggest that the functionally important residue D276 dissociates more from the nearby K278 in the metal free oxidized form relative to the metal bound form (Fig. S12). This in turn might increase the kinase activity by shifting the pK_a of D276 towards higher values, thus favoring ATP hydrolysis, in line with our kinase assay data for PknG with the RD in different redox states for a more folded/bulky substrate such as PknG1-147 if the RD is in the Zn bound state (SI Fig. S7B, C).

Discussion

Conformation and dynamics of the NORS region and PknG autophosphorylation

Intrinsically disordered proteins (IDPs) or protein regions are typically rich in polar amino acids as well as prolines and show a high net charge (20). PknG1-75 corresponding to the NORS region contains 10 prolines, 10 negatively, and 7 positively charged residues as well as a high content of serines and threonines (5 and 10, respectively) and in line with this the web program FoldIndex (http://bip.weizmann.ac.il/fldbin/findex) predicts it to be natively disordered. Moreover, limited proteolysis of PknG resulted in a fragment lacking the first 73 residues (8). The presented NMR structural and dynamic data for the NORS region (His-PknG1-75, Fig. 1C-D and SI Fig. S2-S3A) demonstrate that the NORS region is indeed rather unstructured and dynamic. Since the spectral appearance of the isolated NORS is about the same as connected to the RD (Fig. 3A, SI Fig. S1), the two regions behave rather independent and appear not to interact. Autophosphorylation of the NORS region has been shown to play a role for the survival function of PknG (10) and some IDPs fold upon phosphorylation (20,21). Based on the chemical shift changes of several residues near the phosphorylated threonines observed in the presented NMR monitored kinase assays using as substrates His-PknG1-147 (NORS-RD, Fig. 2B) or His-PknG1-75 (NORS, SI Fig. S7D), phosphorylation appears not to result in global folding but only in local structural changes and it appears not to induce interactions with the subsequent RD. Since phosphorylation modulates locally the charge as well as conformational dynamics (20,22), it may play a role for the interaction with regulatory proteins and/or the KD or the TPRD of the same PknG molecule or a neighboring one or modulate the substrate specificity. One publication describes PknG self-cleavage that results in a fragment encompassing the NORS, the RD, and the KD and another one corresponding to the TPRD as well as autophosphorylation in the TPRD (23). However, consistent with phosphorylation data using radio labeled ATP by other groups (11,14), our data (Fig. 2, SI Fig. S7) suggest that deletion of the NORS region significantly reduces the catalytic activity and that autophosphorylation only occurs if the NORS region is present and thus in the NORS region.

The role of the redox-sensitive RD conformation for the substrate access to the PknG KD

In the crystal structure of PknG74-750 (RD-KD-TPRD) in complex with the small molecule inhibitor AX20017 (PDB-ID 2PZI, Fig. 1B), the RD interacts with both the N- and C-terminal lobes of the kinase domain and packs on top of the ATP binding and catalytic cleft without blocking its access (8). In the crystal structures of PknG74-405 (RD-KD) in complex with ADP-Mg^{2+} (PDB-ID 4Y0X, SI Fig. S6A) or ATP-γS-Mg^{2+} (PDB-ID 4Y12, SI Fig. S6A), the orientation of the RD is slightly different and it makes only contacts to the N-terminal kinase lobe (14). Based on these observations the authors suggested that the RD, in the folded metal bound state, may regulate the catalytic activity by opening and closing the access to the substrate site (14). However, the rather small changes in the orientation of the RD relative to the kinase domain in the inhibitor bound form and the nucleotide bound forms appears not enough to explain the redox regulation of the KD by the RD. It can also not explain the inhibitory effect of AX20017, since this is a consequence of it binding to the active site. The small differences in the orientation of the RD relative to the KD in the different crystal structures arise mostly from small conformational differences due to the presence of different size molecules in the ATP-binding region (AX20017 in 2PZI versus ADP-Mg^{2+} in

4Y0X or ATP-γS-Mg^{2+} in 4Y12) as well as the presence (2PZI) or absence (4Y0X & 4Y12) of the TPRD and different crystallization conditions resulting in different crystal packing. The RD has not only dynamic regions in the isolated state in solution (Fig. 1D, SI Fig. S3A), but shows also in the crystal states rather large stretches with high B factors (SI Fig. S6A). Compared to the inhibitor bound crystal structure (2PZI), the ATP-γS-Mg^{2+} (4Y12) and even more the ADP-Mg^{2+} (4Y0X) bound forms appear overall less flexible (SI Fig. S6A). Thus the observed variation of the orientation of the reduced, metal bound folded RD in the three crystal structures and the observation that it contains dynamic regions in the solution and crystal states suggest that is has enough flexibility to allow binding of substrates. As described for other rubredoxin-like domains or Zn fingers (24,25), the RD only adopts a defined three dimensional fold upon metal binding and the latter has not only a stabilizing effect as for example in the protein IscU (26). Based on the presented NMR, MD, and kinase assay data of the RD in different redox states, the redox regulation of PknG kinase function is rather achieved by redox regulated un- and refolding of the RD, which modulates the substrate access and thus selectivity.

Regulation of PknG catalytic activity by its redox sensitive RD

A redox regulation of the catalytic activity of PknG was initially suggested by kinase assay data for wild type PknG and a mutant in which all 4 cysteines of the RD had been replaced by serines (PknG-C/S). Apparently, this mutant was devoid of catalytic activity towards a substrate corresponding to the N-terminal regions (His-PknG1-147) and that gets phosphorylated in the natively unfolded NORS region (8,10). Tiwari *et al.* used as substrate the FHA domain containing, mostly folded protein GarA and observed the following. Deletion of the NORS and the RD together (PknG151-750) reduces the catalytic activity by ~95 % and mutation of the cysteines in either C-X-X-C-G motif to alanines (C106A/C109A = T1, C128A/C131A = T2) by ~30 % and of both together (T1T2) by ~50-75 %. Moreover, the catalytic activity of the T1T2 mutant was not very sensitive to a shift of the redox conditions (presence of 1 mM reduced or oxidized DTT), whereas wild type PknG showed ~2.5 higher activity under oxidizing conditions (11). The latter is contradictory to the reduction of the catalytic activity by the cysteine to alanine replacements, which should mimic oxidizing, metal releasing conditions. However, addition of oxidized DTT alone may not be sufficient to induce full oxidation of the two C-X-X-C-G motifs of the RD and thus metal release and unfolding and/or the disulfide bonds result in additional local structural order (27,28). Lisa *et al.* used as substrate either GarA or only a 17mer peptide corresponding to GarA residues 14-30. Wild type PknG shows ~45 higher activity towards the folded GarA protein than to the GarA peptide, which with its extended conformation is comparable to an unfolded protein stretch. In addition, the (auto-) phosphorylated NORS region has been suggested to provide pT-dependent anchoring sites for high-affinity interactions with the forkhead-associated (FHA) domain of GarA (29,30). Deletion of the N-terminal 137 residues including the NORS region and most of the RD resulted in higher activity towards the peptide but a bit lower towards the folded GarA protein (14). The latter is in contrast to the data by Tiwari *et al.* (11). As Lisa *et al.* pointed already out, the structural integrity of the deletion mutants has not been tested (14) and deletion of the RD may destabilize the kinase fold stronger than just oxidizing the RD C-X-X-C-G motifs. To complement the published kinase assay data and because PknG autophosphorylation has been shown to be important for mycobacterial survival (10), we used as substrate as Scherr *et al.* (8,10) His-PknG1-147 and as kinase either wild type His-PknG or the deletion mutants His-PknG74-420 (RD-KD) or His-PknG74-750 (RD-KD-TPRD). Based on our data (Fig. 2 and SI Fig. S7), the substrate with the RD in the oxidized, unfolded state is better phosphorylated. This indicates that PknG with the RD in reduced, metal bound, folded state may better phosphorylate substrates with extended structures. Whereas the kinase with the RD in the oxidized unfolded state phosphorylates the substrate His-PknG1-147 with the RD in either redox state about equally well. Since the phosphorylated threonines are located in the mostly unstructured NORS region that adopts overall a more extended peptide like conformation, the redox state of the RD either in the substrate or the kinase is generally expected to have overall a smaller effect than for a larger

folded substrate. Interestingly, in the work of Tiwari *et al*. (11) the PknG mutant with all four cysteines of the RD C-X-X-C-G motifs replaced by alanines showed still significant activity, whereas the one with all replaced to serines in the work by Scherr *et al.* showed no activity (8). Based on our kinase assays under different redox conditions, the results by Tiwari make more sense since mutagenesis of the cysteines should just have a similar effect as oxidative unfolding. Although there are some contradictory results regarding the catalytic activity of PknG under different redox conditions and for different mutants that arise from differences in the used buffer conditions (amount of substrate, kinase, 'hot' and 'cold' ATP, Mg and Mn salts, type of reducing/oxidizing agent and other) and the used substrates (GarA, GarA peptide, His-PknG1-147, or kinase dead PknG-K181M) (8,10,11,14), the data altogether suggest that deletion of the RD or mutation of the cysteines in the two RD C-X-X-C-G motifs and changes in the redox conditions affect the kinase function of PknG. Based on the provided NMR and MD data about redox induced conformational changes in PknG (Fig. 3, SI Fig. S3B, S8, S10-S12) and the functional data (Fig. 2, SI Fig. S7), however rather by modulating its substrate selectivity than by modulating its intrinsic catalytic efficiency.

Modulation of PknG function by reactive oxidative species (ROS) in the host cell

The presented NMR and MD structural and dynamic data suggest that the function of PknG can be modulated by oxidative unfolding of the redox sensitive RD, which makes the catalytic cleft more accessible for substrates (Fig. 3, SI Fig. S3B, S8, S10-S12). Similar redox-sensitive regulation mechanisms involving a four-cysteine ($ZnCys_4$) or two-cysteine-two-histidine ($ZnCys_2His_2$) metal center have for example been proposed for the heat shock protein 33 (Hsp33) and the mycobacterial σ-factor binding protein RslA, respectively (27,31). Other examples are the anti-σ-factors RsrR ($ZnCys_3His$) and ChrR ($ZnCys_2His_2$) that regulate bacterial defense against oxygen and disulfide stress (28,32,33). Oxidative unfolding of the PknG RD in our study has been achieved using a combination of hydrogen peroxide (H_2O_2) and a metal chelator (EDTA). The degree of oxidation and metal release depend further on other conditions such as the pH or the temperature (28). For example for Hsp33, H_2O_2 alone is also not enough to induce oxidation and metal release. Full activation of Hsp33 requires either a combination of H_2O_2 and elevated temperatures (43 °C) or the stronger oxidant hypochlorous acid (HOCl) (27). Cells of the host innate immune system such as macrophages produce high concentrations of reactive oxygen species (ROS) such as hydrogen peroxide (H_2O_2), superoxide (O_2^-), or hypochlorous acid (HOCl) and release them into the phagosome to kill engulfed pathogenic organisms (17,34). PknG is secreted into the host cell, where it can be localized in the cytosol and the phagosome (9). Since blocking of the phagosome-lysosome fusion and thus mycobacterial killing affords the catalytic activity of PknG, the proposed regulation of PknG activity and/or substrate specificity by oxidative unfolding of its RD makes completely sense. Future studies have to answer the question, if PknG autophosphorylation promotes mycobacterial survival in the host by just affecting its interaction with host proteins or also by phosphorylating host proteins in the cytosol and/or phagosome. One target in the host is the protein kinase C-α, a regulator of phagocytosis and the biogenesis of the phagolysosome and the closest human homologue of PknG (34,35). PknG has been proposed to downregulate protein kinase C-α by stimulating its degradation and to be *in vitro* able to proteolytically cleave but not phosphorylate it (35). Future studies have to address the question if other proteins in the host cell are targeted, which are most likely also involved in controlling the phagosome-lysosome fusion, and how exactly PknG interacts with them to modulate host signaling, involving for example interactions of the autophosphorylated NORS region with FHA domains of human target proteins similar to those with the mycobacterial substrate protein GarA (29,30).

Experimental procedures

Cloning and mutagenesis

Expression plasmids (pET-15b) for His-tagged PknG1-750 (wild type, NORS-RD-KD-TPRD, Fig. 1A) as well as PknG1-147 (NORS-RD) and PknG74-750 (RD-KD-TPRD) were kindly provided by the group of Prof. Dr. Jean Pieters from the Biozentrum of the University of Basel. Expression plasmids pET-15b::PknG1-75 and pET-15b::PknG74-147 were obtained by a

mutagenesis based approach as described earlier (15). The quadruple mutant His-PknG1-147-4C/4S, in which C106, C109, C128, and C131 are replaced by serines and the expression plasmid His-PknG74-420 (RD-KD) that was derived from the one for His-PknG74-750 by introducing a stop codon at position 421 were prepared using the QuikChange site-directed mutagenesis method (Stratagene, La Jolla, CA).

Protein expression and purification

Protein expression and purification of His-PknG1-147, His-PknG1-75, and PknG74-147 were carried out as described previously (15). All proteins were overexpressed in *Escherichia coli* BL21 (DE3) cells (Novagen). Following induction with IPTG, cells were grown for 16 h at 15 °C, whereas for the expression of PknG1-147-4C/4S cells were grown for 2 h at 37 °C. For *in vitro* kinase assays His-PknG1-750, His-PknG74-750, and His-PknG74-420 were expressed in rich medium (LB). For NMR measurements His-PknG1-75, His-PknG1-147, and PknG74-147 were expressed in ^{15}N- or ^{15}N-^{13}C-enriched M9 minimal medium (36) supplemented with 1x BME vitamin solution (Sigma) and trace elements as described previously (15). His-PknG74-420 was expressed in ^{15}N-enriched M9 minimal medium containing 70 % D_2O. Cells were harvested by centrifugation, sonicated, and the supernatant after centrifugation loaded on a gravity flow column filled with Ni-NTA agarose beads (Qiagen). Fractions containing significant amounts of PknG1-750, PknG74-750, or PknG74-420 were pooled, concentrated, and further purified by size exclusion chromatography using a 200 pg Superdex^{TM} HiLoad^{TM} 16/600 column equilibrated in 20 mM Tris, 500 mM NaCl, pH 7.5. Fractions containing the target protein were pooled and concentrated using Amicon® Ultra centrifugal filter units (MWCO 10 kDa). All purification steps were carried out at 4 °C. Following Ni-affinity chromatography, fractions containing the mutant His-PknG1-147-4C/4S were loaded on a semi-preparative C4 column (Jupiter® 5 µm C4, 300 Å, 250 × 10 mm, Phenomenex) and eluted using a linear gradient from 10 to 90 % buffer B (buffer A: H_2O with 0.1 % TFA, buffer B: 90 % acetonitrile, 10 % H_2O with 0.1 % TFA) with a flow rate of 4 ml/min within 70 minutes. The purified protein was lyophilized, dissolved in NMR buffer (20 mM Tris, 150 mM NaCl, pH 7.5), washed and concentrated using Amicon® Ultra centrifugal filter units (MWCO 10 kDa).

In vitro phosphorylation observed using a PhosphorImager

In vitro kinase assays were performed as 25 µl reactions in 20 mM Tris (pH 7.5) supplemented with 150 mM NaCl, 10 mM $MgCl_2$, 2 mM $MnCl_2$, and 40 µM [γ-^{32}P] ATP with an activity of 0.5 µCi. For the activity measurements 0.6 µM kinase (His-PknG1-750 or His-PknG74-750 or His-PknG74-420) and a 5-fold molar excess of substrate (His-PknG1-147) were incubated at 30 °C for 30 minutes. The kinase reaction was stopped by adding 6x SDS PAGE sample buffer and boiling of the sample at 95 °C for 10 minutes. The kinase and/or the substrate with the RD in the oxidized form were obtained by adding a 40-fold molar excess of H_2O_2 and EDTA and incubation at 4 °C overnight. The next morning a buffer exchange was carried out using a gravity flow Superdex^{TM} G-25 M PD-10 column (GE-Healthcare). Afterwards the protein solution was concentrated using Amicon® Ultra centrifugal filter devices (MWCO 10 kDa) at 10k rpm and 4 °C. Aliquots taken during the kinase assays were separated by SDS-PAGE using 15 % polyacrylamide gels. Phosphorylation of the substrate was detected by applying a phosphor image screen onto the gel using a Typhoon 9200 PhosphorImager. The analysis of the kinase assay data was done with the program ImageQuant (GE Healthcare).

In vitro phosphorylation observed by NMR

NMR samples used to monitor substrate phosphorylation based on ^{1}H-^{15}N-HSQC spectra contained 0.1 mM of ^{15}N-His-PknG1-75 or 1-147 (substrate) in the presence of 1 mM ATP and 5 mM $MgCl_2$ in 20 mM Tris (pH 7.5), 150 mM NaCl, 0.05 % NaN_3, 5 % D_2O, and 10 µM of unlabeled, catalytic active His-PknG74-420. Consecutive spectra were acquired at 298 K on a Bruker Avance 500 MHz spectrometer equipped with a cryogenic probe. Overnight incubation of the NMR sample at 310 K was done using a thermostated water bath.

NMR sample preparation (without kinase assays)

The protein concentration of the ^{15}N- and ^{15}N-^{13}C-labeled samples of His-PknG1-75, PknG74-147, and His-PknG1-147 in 20 mM Tris (pH 7.5), 150 mM NaCl (95 % H_2O, 5 % D_2O)

ranged from 0.1-0.8 mM. The sample of ^{15}N-^{13}C-PknG74-147 (0.2 mM) for measuring residual dipolar couplings contained ~17 mg/ml PF1 phages (ASLA Biotech). The protein concentration of ^{15}N-D-PknG74-420 in 20 mM Tris (pH 7.5), 500 mM NaCl, 10 mM TCEP, 0.5 mM $MgCl_2$, and 0.5 mM ATP was 0.1 mM.

NMR spectroscopy

NMR spectra were acquired at 298 K on Bruker Avance 500, 600, and 900 MHz spectrometers, the 500 and 900 MHz ones equipped with cryogenic probes. The data were processed with NMRPipe (37) and analyzed using NMRView (38). Assignments for ^{13}C, ^{15}N, and ^{1}H nuclei were based on three-dimensional constant-time HNCA, CBCANH, CCONH-TOCSY, and HNCO spectra as described previously (39). The assigned chemical shifts have been deposited at the BMRB (accession numbers 26028 for the His-PknG1-147 with the RD in reduced, metal bound state, 26027 for His-PknG1-75, 26030 and 26029 for PknG74-147 either in the reduced, metal bound or oxidized state, respectively) (39). The $^{13}C^{\alpha}$ and $^{1}H^{\alpha}$ secondary shifts were calculated as the difference between the measured chemical shift value and the random coil value for the respective amino acid (40). $^{3}J_{HNH\alpha}$ coupling constants were obtained from three-dimensional HNHA spectra (41).

Information about the backbone dynamics were derived from ^{15}N relaxation data including T_1 (spin-lattice relaxation), T_2 (spin-spin relaxation), and ^{1}H-{^{15}N}-NOE. ^{15}N-^{1}H residual dipolar couplings were obtained from the analysis of ^{15}N-^{1}H-IPAP-HSQC data (42). The maximal $^{1}D_{N\text{-}H}$ for PknG74-147 was 15.7 Hz.

Molecular dynamics simulations

Full atomistic molecular models of PknG74-420 with the RD in the Fe^{2+} and oxidized states were constructed based on the crystal structure of PknG74-750 in complex with the inhibitor AX20017 (PDB ID: 2PZI) (8). The loops missing in the crystal structure were modeled using ModLoop (43). The models were solvated in a water box with Na^{+}/Cl^{-} ions, mimicking a 100 mM salt concentration. The molecular systems comprising *ca*. 62'500 atoms, were simulated in an *NPT* ensemble at T = 310 K and p = 101.3 kPa for 250 ns, using a 2 fs integration time steps, and treating long-range electrostatic effects using the Particle Mesh Ewald (PME) approach. Three MD simulations for each state, in total 1.5 ms, were performed in NAMD 2.9 (44) using the CHARMM27 force field (45) and force field parameters for the Fe^{2+}-4Cys center obtained from the literature (46). Visual Molecular Dynamics (VMD) (47) was used for analyzing of the MD trajectories, and cavity volumes were calculated using the *fpocket* package (48). The average extension of three loops surrounding the ATP-binding site, Loop 1 (residue 94-105), Loop 2 (residue 292-297) and Loop 3 (residue 298-310), were calculated from the averaged Cα distances between residues $\langle d_{Loop1} \rangle$: T95 and E101, N96 and S102, P97 and K103, and V98 and R104; $\langle d_{Loop2} \rangle$: I292 and G295, D293 and A296, and L294 and V297; $\langle d_{Loop3} \rangle$: S298 and F303; R299 and G304; I300 and Y305; and, N301 and L306.

Acknowledgements

This work was supported by grants from the German Research Foundation (DFG) to SAD (SFB1035, project B04) and VRIK (SFB1035, project B12). SAD acknowledges further financial support from the TUM diversity and talent management office and the Helmholtz portfolio theme 'metabolic dysfunction and common disease' of the Helmholtz Zentrum München. QL acknowledges the China Scholarship Council (CSC) for funding. Computer resources were provided in part by the Gauss Centre for Supercomputing/Leibniz Supercomputing Centre (grant: pr84pa to VRIK). We thank Dr. Nicole Scherr, who did her Ph.D. thesis in the group of Prof. Dr. Jean Pieters, Hélène Rossez, and Prof. Dr. Jean Pieters from the Biozentrum of the University of Basel for providing the expression plasmids for His-tagged PknG1-147, PknG74-750, and PknG1-750 as well as purification protocols. We thank Tobias Bauer, Eugen Dornstauder, and Milica Vunjak for their contributions while they were doing practical and/or a thesis project in our group. Prof. Dr. Michael Sattler and Prof. Dr. Bernd Reif from the TU München and Helmholtz Zentrum München we thank very much for hosting our group and for continuous support as well as for sharing their facilities with us.

Conflict of interest

The authors declare that they have no conflicts of interest with the contents of this article.

Author contributions

SAD designed and coordinated the study, helped acquiring and analyzing the NMR data, and wrote the paper. MW designed, performed, and analyzed the NMR and kinase assay data shown in Figures 1-3 and supplementary Figures S1-S9, and helped writing the manuscript. QL designed, performed, and analyzed the molecular dynamics simulation data shown in Figure 3 and supplementary Figures S10-S12 as well as supplementary Table S1. VRIK designed and coordinated the molecular dynamics part of the study and wrote the corresponding part of the paper. All authors reviewed the results and approved the final version of the manuscript.

References

1. Bhat, S. A., Singh, N., Trivedi, A., Kansal, P., Gupta, P., and Kumar, A. (2012) The mechanism of redox sensing in Mycobacterium tuberculosis. *Free radical biology & medicine* **53**, 1625-1641
2. Chim, N., Johnson, P. M., and Goulding, C. W. (2014) Insights into redox sensing metalloproteins in Mycobacterium tuberculosis. *Journal of inorganic biochemistry* **133**, 118-126
3. Kumar, A., Farhana, A., Guidry, L., Saini, V., Hondalus, M., and Steyn, A. J. (2011) Redox homeostasis in mycobacteria: the key to tuberculosis control? *Expert reviews in molecular medicine* **13**, e39
4. Sureka, K., Hossain, T., Mukherjee, P., Chatterjee, P., Datta, P., Kundu, M., and Basu, J. (2010) Novel role of phosphorylation-dependent interaction between FtsZ and FipA in mycobacterial cell division. *PloS one* **5**, e8590
5. Park, S. T., Kang, C. M., and Husson, R. N. (2008) Regulation of the SigH stress response regulon by an essential protein kinase in Mycobacterium tuberculosis. *Proceedings of the National Academy of Sciences of the United States of America* **105**, 13105-13110
6. Av-Gay, Y., and Everett, M. (2000) The eukaryotic-like Ser/Thr protein kinases of Mycobacterium tuberculosis. *Trends in microbiology* **8**, 238-244
7. Jayakumar, D., Jacobs, W. R., Jr., and Narayanan, S. (2008) Protein kinase E of Mycobacterium tuberculosis has a role in the nitric oxide stress response and apoptosis in a human macrophage model of infection. *Cellular microbiology* **10**, 365-374
8. Scherr, N., Honnappa, S., Kunz, G., Mueller, P., Jayachandran, R., Winkler, F., Pieters, J., and Steinmetz, M. O. (2007) Structural basis for the specific inhibition of protein kinase G, a virulence factor of Mycobacterium tuberculosis. *Proceedings of the National Academy of Sciences of the United States of America* **104**, 12151-12156
9. Walburger, A., Koul, A., Ferrari, G., Nguyen, L., Prescianotto-Baschong, C., Huygen, K., Klebl, B., Thompson, C., Bacher, G., and Pieters, J. (2004) Protein kinase G from pathogenic mycobacteria promotes survival within macrophages. *Science* **304**, 1800-1804
10. Scherr, N., Muller, P., Perisa, D., Combaluzier, B., Jeno, P., and Pieters, J. (2009) Survival of pathogenic mycobacteria in macrophages is mediated through autophosphorylation of protein kinase G. *Journal of bacteriology* **191**, 4546-4554
11. Tiwari, D., Singh, R. K., Goswami, K., Verma, S. K., Prakash, B., and Nandicoori, V. K. (2009) Key residues in Mycobacterium tuberculosis protein kinase G play a role in regulating kinase activity and survival in the host. *The Journal of biological chemistry* **284**, 27467-27479
12. Sieker, L. C., Stenkamp, R. E., and LeGall, J. (1994) Rubredoxin in crystalline state. *Methods in enzymology* **243**, 203-216

13. Dauter, Z., Wilson, K. S., Sieker, L. C., Moulis, J. M., and Meyer, J. (1996) Zinc- and iron-rubredoxins from Clostridium pasteurianum at atomic resolution: a high-precision model of a ZnS4 coordination unit in a protein. *Proceedings of the National Academy of Sciences of the United States of America* **93**, 8836-8840
14. Lisa, M. N., Gil, M., Andre-Leroux, G., Barilone, N., Duran, R., Biondi, R. M., and Alzari, P. M. (2015) Molecular Basis of the Activity and the Regulation of the Eukaryotic-like S/T Protein Kinase PknG from Mycobacterium tuberculosis. *Structure* **23**, 1039-1048
15. Wittwer, M., and Dames, S. A. (2015) Expression and purification of the natively disordered and redox sensitive metal binding regions of Mycobacterium tuberculosis protein kinase G. *Protein expression and purification* **111**, 68-74
16. Gil, M., Grana, M., Schopfer, F. J., Wagner, T., Denicola, A., Freeman, B. A., Alzari, P. M., Batthyany, C., and Duran, R. (2013) Inhibition of Mycobacterium tuberculosis PknG by non-catalytic rubredoxin domain specific modification: reaction of an electrophilic nitro-fatty acid with the Fe-S center. *Free radical biology & medicine* **65**, 150-161
17. Miller, R. A., and Britigan, B. E. (1997) Role of oxidants in microbial pathophysiology. *Clinical microbiology reviews* **10**, 1-18
18. Shen, Y., and Bax, A. (2010) SPARTA+: a modest improvement in empirical NMR chemical shift prediction by means of an artificial neural network. *Journal of biomolecular NMR* **48**, 13-22
19. Dames, S. A., Aregger, R., Vajpai, N., Bernado, P., Blackledge, M., and Grzesiek, S. (2006) Residual dipolar couplings in short peptides reveal systematic conformational preferences of individual amino acids. *J Am Chem Soc* **128**, 13508-13514
20. Dunker, A. K., Bondos, S. E., Huang, F., and Oldfield, C. J. (2015) Intrinsically disordered proteins and multicellular organisms. *Seminars in cell & developmental biology* **37**, 44-55
21. Bah, A., Vernon, R. M., Siddiqui, Z., Krzeminski, M., Muhandiram, R., Zhao, C., Sonenberg, N., Kay, L. E., and Forman-Kay, J. D. (2015) Folding of an intrinsically disordered protein by phosphorylation as a regulatory switch. *Nature* **519**, 106-109
22. Tharun, I. M., Nieto, L., Haase, C., Scheepstra, M., Balk, M., Mocklinghoff, S., Adriaens, W., Dames, S. A., and Brunsveld, L. (2015) Subtype-specific modulation of estrogen receptor-coactivator interaction by phosphorylation. *ACS chemical biology* **10**, 475-484
23. Cowley, S., Ko, M., Pick, N., Chow, R., Downing, K. J., Gordhan, B. G., Betts, J. C., Mizrahi, V., Smith, D. A., Stokes, R. W., and Av-Gay, Y. (2004) The Mycobacterium tuberculosis protein serine/threonine kinase PknG is linked to cellular glutamate/glutamine levels and is important for growth in vivo. *Molecular microbiology* **52**, 1691-1702
24. Zheng, P., Wang, Y., and Li, H. (2014) Reversible unfolding-refolding of rubredoxin: a single-molecule force spectroscopy study. *Angewandte Chemie* **53**, 14060-14063
25. Dames, S. A., Martinez-Yamout, M., De Guzman, R. N., Dyson, H. J., and Wright, P. E. (2002) Structural basis for Hif-1 alpha /CBP recognition in the cellular hypoxic response. *Proceedings of the National Academy of Sciences of the United States of America* **99**, 5271-5276
26. Iannuzzi, C., Adrover, M., Puglisi, R., Yan, R., Temussi, P. A., and Pastore, A. (2014) The role of zinc in the stability of the marginally stable IscU scaffold protein. *Protein science : a publication of the Protein Society* **23**, 1208-1219
27. Winter, J., Ilbert, M., Graf, P. C., Ozcelik, D., and Jakob, U. (2008) Bleach activates a redox-regulated chaperone by oxidative protein unfolding. *Cell* **135**, 691-701

28. Bourles, E., Isaac, M., Lebrun, C., Latour, J. M., and Seneque, O. (2011) Oxidation of Zn(Cys)4 zinc finger peptides by O2 and H2O2: products, mechanism and kinetics. *Chemistry* **17**, 13762-13772
29. O'Hare, H. M., Duran, R., Cervenansky, C., Bellinzoni, M., Wehenkel, A. M., Pritsch, O., Obal, G., Baumgartner, J., Vialaret, J., Johnsson, K., and Alzari, P. M. (2008) Regulation of glutamate metabolism by protein kinases in mycobacteria. *Molecular microbiology* **70**, 1408-1423
30. Li, J., Lee, G. I., Van Doren, S. R., and Walker, J. C. (2000) The FHA domain mediates phosphoprotein interactions. *Journal of cell science* **113 Pt 23**, 4143-4149
31. Thakur, K. G., Praveena, T., and Gopal, B. (2010) Structural and biochemical bases for the redox sensitivity of Mycobacterium tuberculosis RslA. *J Mol Biol* **397**, 1199-1208
32. Zdanowski, K., Doughty, P., Jakimowicz, P., O'Hara, L., Buttner, M. J., Paget, M. S., and Kleanthous, C. (2006) Assignment of the zinc ligands in RsrA, a redox-sensing ZAS protein from Streptomyces coelicolor. *Biochemistry* **45**, 8294-8300
33. Campbell, E. A., Greenwell, R., Anthony, J. R., Wang, S., Lim, L., Das, K., Sofia, H. J., Donohue, T. J., and Darst, S. A. (2007) A conserved structural module regulates transcriptional responses to diverse stress signals in bacteria. *Molecular cell* **27**, 793-805
34. Nguyen, L., and Pieters, J. (2005) The Trojan horse: survival tactics of pathogenic mycobacteria in macrophages. *Trends in cell biology* **15**, 269-276
35. Chaurasiya, S. K., and Srivastava, K. K. (2009) Downregulation of protein kinase C-alpha enhances intracellular survival of Mycobacteria: role of PknG. *BMC microbiology* **9**, 271
36. Marley, J., Lu, M., and Bracken, C. (2001) A method for efficient isotopic labeling of recombinant proteins. *Journal of biomolecular NMR* **20**, 71-75
37. Delaglio, F., Grzesiek, S., Vuister, G. W., Zhu, G., Pfeifer, J., and Bax, A. (1995) NMRPipe: a multidimensional spectral processing system based on UNIX pipes. *Journal of biomolecular NMR* **6**, 277-293
38. Johnson, B. A. (2004) Using NMRView to visualize and analyze the NMR spectra of macromolecules. *Methods in molecular biology* **278**, 313-352
39. Wittwer, M., and Dames, S. A. (2016) Chemical shift assignment of the intrinsically disordered N-terminus and the rubredoxin domain in the folded metal bound and unfolded oxidized state of mycobacterial protein kinase G. *Biomol NMR Assign* **10**, 401-406
40. Wishart, D. S., Bigam, C. G., Holm, A., Hodges, R. S., and Sykes, B. D. (1995) 1H, 13C and 15N random coil NMR chemical shifts of the common amino acids. I. Investigations of nearest-neighbor effects. *Journal of biomolecular NMR* **5**, 67-81
41. Vuister, G. W., and Bax, A. (1993) Quantitative J correlation: a new approach for measuring homonuclear three-bond J(HNH.alpha.) coupling constants in 15N-enriched proteins. *Journal of the American Chemical Society* **115**, 7772-7777
42. Ottiger, M., Delaglio, F., and Bax, A. (1998) Measurement of J and dipolar couplings from simplified two-dimensional NMR spectra. *Journal of magnetic resonance* **131**, 373-378
43. Fiser, A., and Sali, A. (2003) ModLoop: automated modeling of loops in protein structures. *Bioinformatics* **19**, 2500-2501
44. Phillips, J. C., Braun, R., Wang, W., Gumbart, J., Tajkhorshid, E., Villa, E., Chipot, C., Skeel, R. D., Kale, L., and Schulten, K. (2005) Scalable molecular dynamics with NAMD. *Journal of computational chemistry* **26**, 1781-1802

45. MacKerell, A. D., Bashford, D., Bellott, M., Dunbrack, R., Evanseck, J., Field, M. J., Fischer, S., Gao, J., Guo, H., and Ha, S. a. (1998) All-atom empirical potential for molecular modeling and dynamics studies of proteins. *The journal of physical chemistry B* **102**, 3586-3616
46. Gámiz-Hernández, A. P., Galstyan, A. S., and Knapp, E.-W. (2009) Understanding rubredoxin redox potentials: role of H-bonds on model complexes. *Journal of chemical theory and computation* **5**, 2898-2908
47. Humphrey, W., Dalke, A., and Schulten, K. (1996) VMD: visual molecular dynamics. *Journal of molecular graphics* **14**, 33-38
48. Le Guilloux, V., Schmidtke, P., and Tuffery, P. (2009) Fpocket: an open source platform for ligand pocket detection. *BMC bioinformatics* **10**, 168
49. Wishart, D. S., and Sykes, B. D. (1994) The 13C chemical-shift index: a simple method for the identification of protein secondary structure using 13C chemical-shift data. *Journal of biomolecular NMR* **4**, 171-180
50. Zweckstetter, M. (2008) NMR: prediction of molecular alignment from structure using the PALES software. *Nature protocols* **3**, 679-690

Figure captions

Figure 1

The no regulatory secondary structure (NORS) region of PknG shows local structural order and the redox-sensitive rubredoxin-like metal binding domain (RD) can also fold in the absence of the catalytic domain. **(A)** Schematic representation of the domain structure of PknG. PknG consists besides the N-terminal NORS region (blue) and subsequent RD (red) of the catalytic kinase domain (KD, yellow), and the tetratricopeptide repeat domain (TPRD, green). **(B)** Ribbon representation of the crystal structure of PknG74-750 (RD-KD-TPRD) in complex with the inhibitor AX20017 (stick representation in green, PDB-ID 2PZI) (8). The domain color coding is the same as in (A). **(C-D)** Analysis of the secondary structure content and backbone dynamics of the N-terminal regions of protein kinase G (PknG) by NMR spectroscopy. **(C)** $^{13}C^{\alpha}$ secondary shifts for His-PknG1-75 (NORS, blue) and PknG74-147 (RD - reduced, metal bound, red) plotted as function of the amino acid sequence (49). Chemical shift values significantly higher than the random coil value indicate the presence of α-helical secondary structure elements and those significantly lower of β-sheets. The secondary structure elements for the RD presented above the sequence were extracted from the crystal structure of PknG74-750 in complex with AX20017 (PDB-ID 2PZI, see (B)) (8). SI Fig. S2A-B show the $^{3}J_{HNH\alpha}$ coupling constants and $^{1}H^{\alpha}$ secondary shifts for both constructs, which are both also sensitive to the secondary structure content, and SI Fig. S2C shows the $^{13}C^{\alpha}$ secondary shifts for His-PknG1-147. **(D)** $\{^{1}H\}$-^{15}N-NOE data for His-PknG1-75 (NORS, red), PknG 74-147 (RD - reduced, metal bound, blue), and His-PknG1-147 (NORS-RD - reduced, metal bound, black) plotted as a function of the residue sequence position. Negative to slightly positive values indicate flexible, unstructured regions, whereas positive values around 0.4-0.8 indicate well structured regions. The respective ^{15}N-T_1 as well as -T_2 values are shown in SI Fig. S3A. **(E)** Comparison of the structures of the isolated metal bound rubredoxin-like domain in solution and in the crystal structures of PknG fragments containing additionally the kinase domain. The experimental residual dipolar couplings (RDCs) for the Zn^{2+} bound rubredoxin domain (RD, black symbols) and those back calculated based on the three published crystal structures of PknG using the software PALES (50) were plotted as a function of the sequence position. The back calculated RDCs based on the Cd^{2+} bound RD in PknG74-750 in complex with the inhibitor AX20017 (PDB-ID 2PZI) (8) are represented as green symbols, those of the Zn^{2+} bound RD of PknG74-405 in complex with an ATP analogue (PDB-ID 4Y12) (14) as red symbols and in complex with ADP (PD-ID 4Y0X) (14) as blue symbols. A comparison of the experimental $^{13}C^{\alpha}$ secondary shifts chemical shift values for the metal bound RD with those back calculated based on the published crystal structure data can be found in SI Fig. S4. Plots of the experimental versus calculated RDC values for each crystal structure and a larger

representation of the RD structure as well as ribbon representations of the RD-KD part of each crystal structure are shown in SI Fig. S6. A superposition of the ^{1}H-^{15}N-HSQC spectra of PknG74-147 and His-PknG74-420 in complex with ATP is shown in SI Fig. S5.

Figure 2

PknG catalytic activity is sensitive to the folding state of the substrate and autophosphorylation of the NORS region does not induce global folding. **(A)** Comparison of the phosphorylation activity of His-PknG wild type (wt, blue bars) and the PknG deletion mutants (His-PknG74-750 green bars, His-PknG74-420 red bars, all with the RD in the reduced, metal bound state = RD/Zn) towards the substrate His-PknG1-147 with the RD in the reduced, metal bound (= RD/Zn) or oxidized state (= RD/ox) based on phosphorimager data. The data for the wild type enzyme includes the phosphorylation in trans of its own N-terminus (SI Fig. S7A). Kinase activity data of His-PknG wild type and of an N-terminal truncated version (His-PknG74-750) under different redox conditions and thus with the own RD in reduced/metal bound or oxidized state can be found in SI Fig. S7B and C. **(B)** NMR monitoring of *in vitro* ^{15}N-His-PknG1-147 phosphorylation by His-PknG74-420, both with the RD in the reduced metal bound form (= RD/Zn), based on the superposition of the ^{1}H-^{15}N-HSQC spectra of unphosphorylated ^{15}N-His-PknG1-147 (black) and after kinase treatment for 3 h at 298 K (red) and further overnight at 310 K (green). A * indicates a peak that appears newly after phosphorylation. Assigned backbone amide crosspeaks that shift or show a change in signal intensity are labeled by the one-letter amino acid code and the sequence position (39). The additional label –sc indicates side chain amide protons. The NMR monitoring of the *in vitro* phosphorylation of ^{15}N-His-PknG1-75 is shown in SI Fig S7D.

Figure 3

Redox regulated folding and unfolding of the rubredoxin-like domain of *M. tuberculosis* PknG modulates the access to the catalytic cleft and thereby catalytic activity and/or substrate specificity. **(A)** Superposition of the ^{1}H-^{15}N-HSQC spectra of His-PknG1-147 in the reduced, metal bound form (black) and the oxidized form (red). Assignments for some well resolved peaks are labeled by the one-letter amino acid code and the sequence position (39). The additional label –sc indicates side chain amide protons. Indicated the by the low chemical shift dispersion of all resonances under oxidizing conditions, the oxidized RD is unfolded **(B)** Proposed unfolding and refolding of the RD of PknG by redox changes based on the presented NMR data in (A) and SI figures S3B and S8. **(C-F)** Characterization of conformational changes in the RD and the KD upon oxidation of the two RD C-X-X-C-G motifs (in green) from classical atomistic MD simulations. **(C)** The last snapshots from two 250 ns MD simulations of PknG74-420 with the cysteines of the two C-X-X-C-G motifs of the RD in the reduced state and coordinating Fe^{2+} (Fe^{2+} bound) or in the oxidized state with disulfide bridges between C106 and C109, and C128 and C131 (oxidized). A similar representation for all three runs for each redox state is shown in SI Fig. S10A. The core RD region (residues ~100-140) is shown in red. Atoms within 5 Å of ATP and Mg^{2+} forming the binding cavity are shown in a space filling representation in cyan to indicate that the cavity is more restricted in the Fe^{2+} bound form. **(D)** The structure of three loops surrounding the ATP-binding site, Loop 1 (RD residues 94-105, in blue), Loop 2 (KD residues 292-297, in cyan) and Loop 3 (KD residues 298-310, in magenta) in the Fe^{2+} bound and the oxidized state. The average distribution of the loop extension for Loop 1 **(E)** and Loop 3 **(F)** calculated from three independent 250 ns MD simulations of the Fe^{2+} bound (in blue) and oxidized (in red) states. The distributions suggest that Loop 1 **(E)** and Loop 3 **(F)** become more extended in the oxidized state relative to the Fe^{2+} bound state, leading to opening of the ATP-binding cavity. Loop 2 is not affected by the RD oxidization in the MD simulations (SI Fig. S10B). Plots of the volume of the ATP binding cavity (see also table S1 for average values for the last 50 ns) and the solvent accessible surface area (SASA) of residues interacting with ATP as a function of the simulation time are shown in SI Fig. S11 and stick representations of the region around ATP-Mg^{2+} as well as plots of the distance between D293 and Mg^{2+} as well as D276 and K278 as a function of the simulation time in SI Fig. S12.

Wittwer et al.
Fig. 1

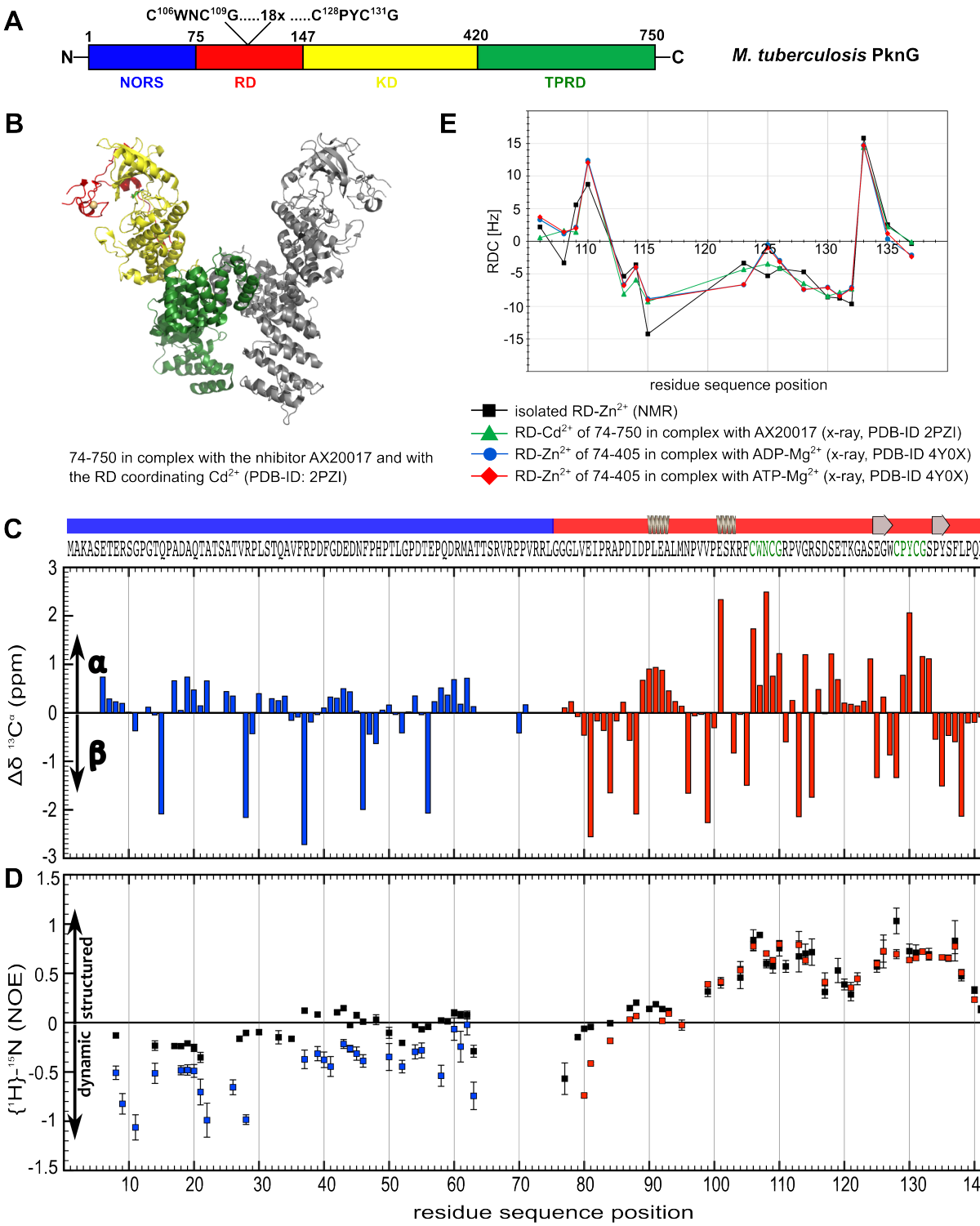

Wittwer et al.
Fig. 2

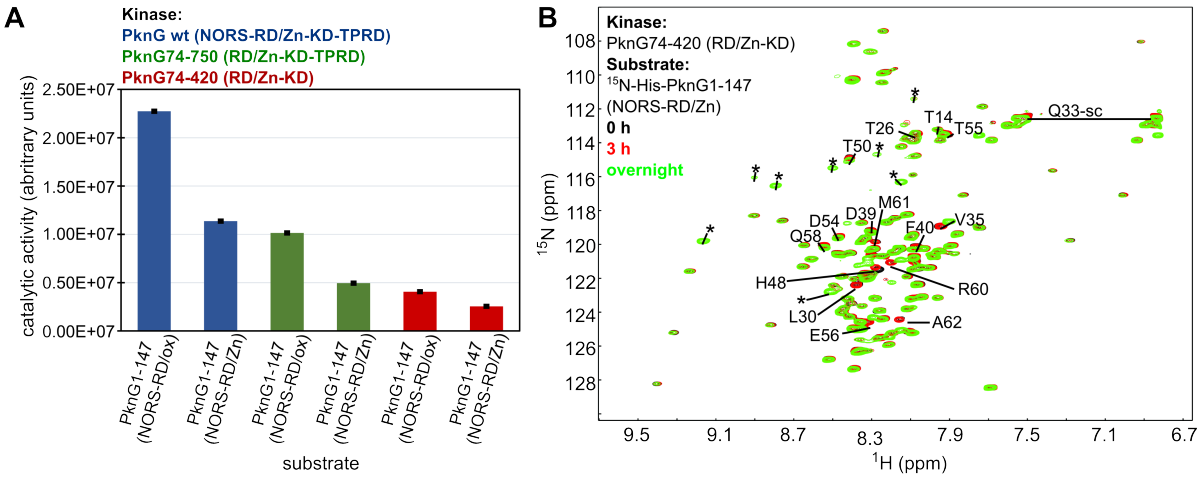

Wittwer et al.
Fig. 3

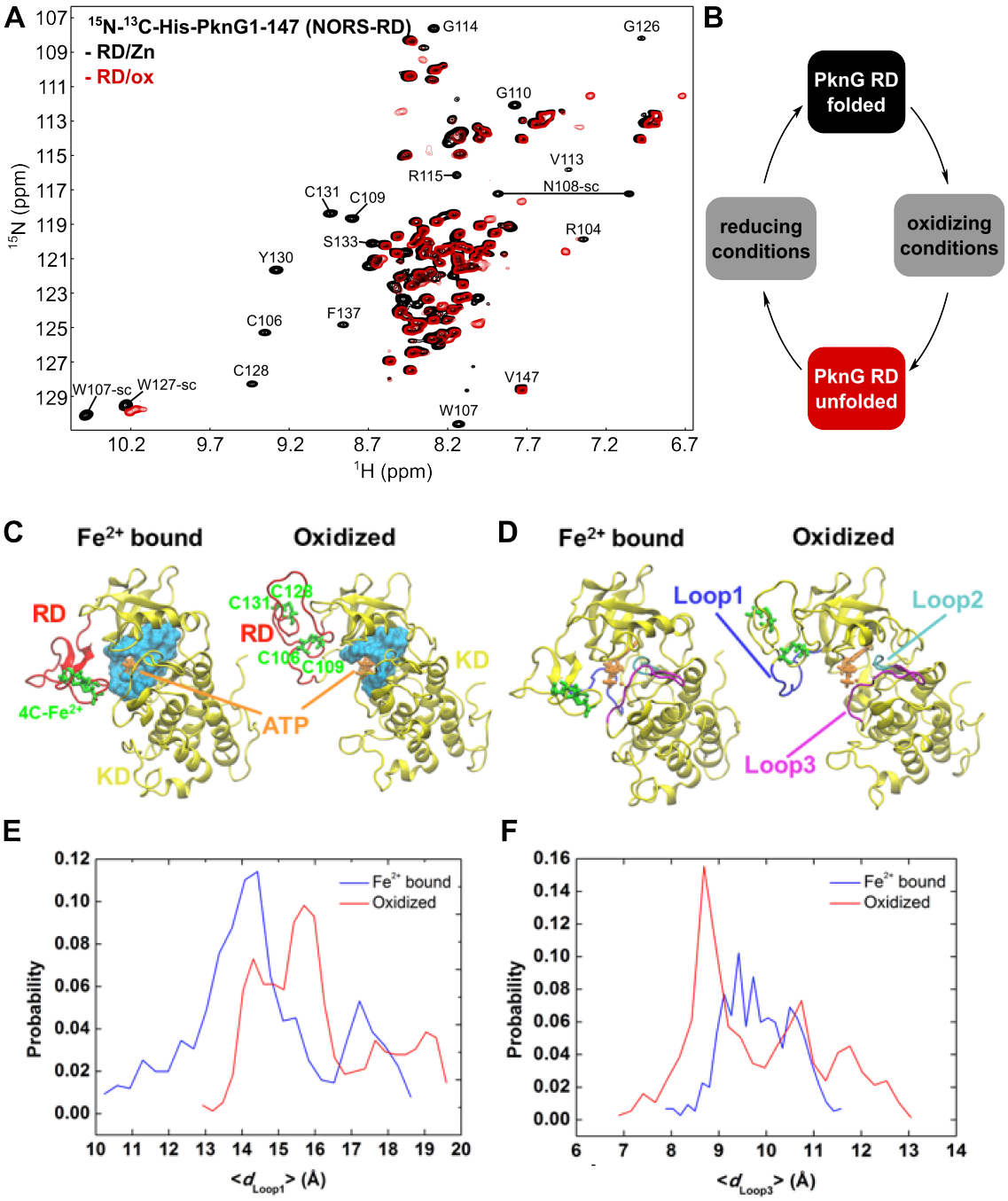

Oxidative unfolding of the rubredoxin domain and the natively disordered N-terminal region regulate the catalytic activity of *M. tuberculosis* protein kinase G

Matthias Wittwer[1a], Qi Luo[1b,2], Ville R. I. Kaila [1b], and Sonja A. Dames[1a,3§]

[1a/b]Technische Universität München, Department of Chemistry, [a]Biomolecular NMR Spectroscopy/[b]Computational Biocatalysis, Lichtenbergstr. 4, 85747 Garching, Germany

[2]Soft Matter Research Center and Department of Chemistry, Zhejiang University, 310027, P.R. China

[3]Institute of Structural Biology, Helmholtz Zentrum München, Ingolstädter Landstr. 1, 85764 Neuherberg, Germany

[§]To whom correspondence may be addressed. E-mail: sonja.dames@tum.de

Supplementary Information

Supplementary Results

Characterization of the backbone dynamics of the PknG N-terminal regions based on ^{15}N-relaxation data

The backbone dynamics of the isolated intrinsically disordered NORS region (His-PknG1-75), the isolated reduced, metal bound folded RD (PknG74-147), and of His-PknG1-147 containing both connected were studied by ^{15}N-relaxation experiments. The additive nature of the ^{1}H-^{15}N-HSQC data (Fig. 3A, SI Fig. S1 and S8) indicated that the NORS and the RD region behave rather independently regarding their structural properties and apparently do not interact. Based on the presented relaxation data for the two segment protein His-PknG1-147 (black symbols in Fig. 1D and SI Fig. S3A) as well as those for each region separately (blue symbols for His-PknG1-75 and red symbols PknG74-147 in Fig. 1D and SI Fig. S3A), the NORS and RD part tumble rather independently and the glycine-rich sequence (G74-G76) connecting them acts as a flexible linker. The $\{^{1}$H$\}$-^{15}N-NOE values of the reduced, metal bound rather well structured RD are almost the same in the isolated state (PknG74-147) and connected to the NORS region (His-PknG1-147). In the core region of the RD (residues ~100-140: ~0.4-0.8) they are typical for a folded protein. Those of the NORS region are more negative in the absence of the RD indicating greater flexibility. Whereas the unfolded NORS region represents just a rather extended chain, it represents a chain connected on one end to a roughly spherical body if connected to the folded RD. As already expected just based on the increase in molecular weight of the two segment protein His-PknG1-147 (18.001 kDa) compared to the isolated regions, His-PknG1-75 (10.241 kDa) and PknG74-147 (7.948 kDa), the presence of either region influences the ^{15}N-T_1 and -T_2 values of the other by modulating the overall tumbling. However, using a model system based on GB1 domains connected by different linker regions, it has been shown that each domain exhibits different rotational diffusion and alignment properties even if the linker was 18 residues long (1). Moreover, exchange effects arising from motions of the two PknG regions with respect to each other have to be considered. The average ^{15}N-T_1, -T_2 and $\{^{1}$H$\}$-^{15}N NOE values for residues 11-63 of the NORS region are 889 ± 210 ms, 267 ± 68 ms, and -0.56 ± 0.41 for the isolated form (blue symbols) and 795 ± 67 ms, 154 ± 32 ms, and -0.07 ± 0.14 if connected to the RD (black symbols), respectively. The average ^{15}N-T_1, -T_2 and $\{^{1}$H$\}$-^{15}N NOE values for residues 101-140 of the folded RD region are 635 ± 50 ms, 55 ± 22 ms, and 0.61 ± 0.15 for the isolated form (red symbols) and 749 ± 80 ms, 48 ± 31 ms, and 0.62 ± 0.19 if connected to the NORS region (black symbols), respectively. The ^{15}N-T_1 values for the isolated RD and

NORS region are about in the range expected for molecules with a size of about 8-10 kDa. The fact that they remain rather similar and do not significantly increase due the increase in molecular weight can be explained by the fact that they are flexibly linked. The ^{15}N-T_2 values for the unfolded NORS region decrease strongly due to presence of the RD, which changes the rotational diffusion properties. As mentioned above, movements of the two segments with respect to each other may result in an additional conformational exchange contribution. The ^{15}N-T_2 values for the folded RD (SI Fig. S3A) are a bit higher if connected to the NORS region. Overall they are significantly lower than expected for a completely unhindered isotropic reorientation of an ~8 kDa protein. Additional exchange effects for the RD arise from local conformational exchange processes within the RD that are also reflected in the {^{1}H}-^{15}N NOE values (Fig. 1D), e.g. residues 117-125 and that are consistent with local increased backbone dynamics indicated by higher B-factors in the available crystal structures of PknG fragments containing the RD (SI Fig. S6A). In addition the RD may experience a viscous drag due to the presence of the unfolded NORS region. A similar effect has been observed for the N-terminal domain of Formin C that contains a large unstructured loop (2).

For the isolated RD in the oxidized, unfolded state we just recorded {^{1}H}-^{15}N NOE data (SI Fig. S5B). Indicated by negative or not visible peaks in the NOE spectrum compared to the reference spectrum, this state shows NOE values that are around 0 or negative consistent with a rather unstructured and dynamic character.

Comparison of the oxidized metal free rubredoxin-like domain in the presence of different metal ions

Rubredoxins are redox sensitive metal binding proteins or protein domains, which can tetrahydrally coordinate metal ions like iron, zinc, cobalt, and cadmium by two C-X-X-C-G motifs (3). The fold and secondary structure content of the RD in the published crystal structures of protein kinase G with the rubredoxin-like domain in complex with Cd^{2+} or Zn^{2+} are very similar (4,5). SI Fig. S9 shows superpositions of the ^{1}H-^{15}N-HSQC spectra of the metal free state and different metal bound states of ^{15}N-His-PknG1-147 that confirm that the rubredoxin-like domain of PknG can also interact with various metal ions. The ^{1}H-^{15}N-HSQC spectrum of the oxidized metal free state (black) is characterized by a low signal dispersion typical for an unfolded protein. Addition of a 4-fold molar excess of a reducing agent such as TCEP and a 3 fold molar excess of Mn^{2+}, Co^{2+}, or Fe^{3+} ions results in the disappearance or shift of several resonances. Compared to the spectra of the Zn^{2+} form, fewer well dispersed peaks are visible. This is due to the paramagnetic relaxation enhancement (PRE) experienced

by the nuclei in the proximity of the metal. Addition of Mn^{2+} (SI Fig. S9A) results in the disappearance of several backbone amide crosspeaks ~7.7–8.7 ppm, however the peaks for the side amides of the two tryptophans (~10 ppm) appear only to show a slight decrease in intensity. The Co^{2+} bound form shows at least a few well dispersed backbone amide crosspeaks ~7.2–7.7 ppm and ~9.5 ppm (SI Fig. S9B). Moreover, the peaks for the side chain amides of the two tryptophans (W107 & W127, ~10 ppm), which are in or sequentially close to the C-X-X-C-G motifs (^{106}C-W-N-C-G^{110} & ^{128}C-P-Y-C-G^{132}) disappear of shift. Addition of Fe^{3+} ions (SI Fig. S9C) results in the disappearance or shift of a few backbone resonances. Although, the originally present peaks for the side chain amides of the two tryptophans (~10 ppm) appear only to show a slight decrease in intensity, clearly a new peak becomes visible ~10.5 ppm. Spectral differences between the different metal bound states may arise from differences in the affinity for the respective metals as well as differences regarding the paramagnetic properties of the coordinated metal.

Supplementary figure legends

Fig. S1: Superposition of the ^{1}H-^{15}N-HSQC spectra of His-PknG1-147 (black), His-PknG1-75 (green), and PknG74-147 (red). The RD was always present in the reduced, metal bound (Zn^{2+}) state. Note that the spectra of His-PknG1-75 (green), and PknG74-147 (red) are almost perfectly additive subspectra of the one of His-PknG1-147 (black). The assignments for His-PknG1-75, which corresponds to the natively disordered NORS region, are indicated by the one letter amino acid code and the sequence positions. The black rectangle contains side chain amide protons of glutamine and asparagine residues. Assignments for the RD can be found in Fig. 3A and SI Fig. S5. The assigned chemical shifts for all have been deposited at the BMRB (accession numbers 26028 for the His-PknG1-147 with the RD in reduced, metal bound state, 26027 for His-PknG1-75, 26030 and 26029 for PknG74-147 either in the reduced, metal bound or oxidized state, respectively) (6).

Fig. S2: More NMR data sensitive to the secondary structure content for the PknG N-terminal regions. **(A)** $^{3}J_{HNH\alpha}$ coupling constants of ^{15}N-His-PknG1-75 (NORS, blue) and ^{15}N-PknG74-147 (RD, red) plotted as a function of the residue sequence position. The data was derived from 3D HNHA spectra. The measured values were corrected by +11 % as suggested in the literature (7). Values below ~6-6.5 Hz are typically observed in α-helical regions, whereas values above ~8-8.5 Hz are characteristic for residues in β-sheets. Values in the

range ~6-8 Hz are typical for protein regions undergoing conformational exchange. The secondary structure elements for the RD presented above of the sequence were extracted from the crystal structure of PknG74-750 in complex with AX20017 (PDB-ID 2PZI, Fig. 1B, SI Fig. S6A) (4). **(B-C)** $^{1}H^{\alpha}$ secondary shifts for His-PknG1-75 (NORS, blue) and PknG74-147 (RD, reduced, metal bound, red) and $^{13}C^{\alpha}$ secondary shifts for the two segment protein His-PknG1-147 (NORS-RD, black) plotted as function of the residue sequence position (8). The $^{13}C^{\alpha}$ secondary shifts for the single region proteins are shown in Fig. 1C. Note, whereas $^{1}H^{\alpha}$ chemical shift values significantly lower than the random coil value indicate the presence of α-helical secondary structure elements and those significantly higher of β-sheets, the behavior is opposite for the $^{13}C^{\alpha}$ chemical shifts.

Fig. S3: (A) Further ^{15}N-relaxation data for ^{15}N-His-PknG1-75 (NORS, blue), ^{15}N-PknG74-147 (RD, reduced, metal bound, red), and ^{15}N-His-PknG1-147 (NORS-RD, reduced, metal bound, black). The top panel shows the ^{15}N-T_1 and the bottom the -T_2 values as a function of the residue sequence position. **(B)** $\{^{1}H\}$-^{15}N-NOE NMR data for PknG 74-147 (RD) in the oxidized, unstructured state. Positive and negative peaks of the reference spectrum are shown in black and blue, respectively, and those of the NOE spectrum in magenta and red, respectively. Red peaks on top of black ones indicate the presence of highly flexible regions with negative NOE values, whereas black peaks with no peak on top indicate less dynamic residues with NOE values around 0. Magenta peaks on top of black peaks indicate residues with positive NOE values typical for more structured regions. Note that the behavior for the side chain amide protons of the tryptophan peaks (^{1}H shift ~10 ppm) is opposite because they are spectrally folded. Assigned backbone amide crosspeaks that shifted or showed a change in signal intensity are labeled by the one-letter amino acid code and the sequence position (6).

Fig. S4: Comparison of the secondary structure content of the isolated PknG RD in solution compared to the three available crystal structures of constructs containing the RD and the kinase domain based on experimental and back calculated $^{13}C^{\alpha}$ secondary shifts. The experimental data for the Zn^{2+} form measured by NMR spectroscopy is shown in the top panel (red bars) (8). $^{13}C^{\alpha}$ secondary shifts based on the published crystal structures were calculated using the program SPARTA+ (9). The second panel (yellow bars) shows the data for the Cd^{2+} bound form of the RD in the structure of PknG74-750 (RD-KD-TPRD) in complex with the inhibitor AX20017 (PDB-ID 2PZI) (4). Those for the Zn^{2+} bound forms of

the RD in the structures of PknG74-405 (RD-KD) in complex with either an ATP analogue (ATP-γS, blue bars, PDB-ID 4Y12) or ADP (green bars, PDB-ID 4Y0X) (5) are shown in the third and fourth panel, respectively. Chemical shift values significantly higher than the random coil value indicate the presence of α-helical structure elements and those significantly lower of β-sheets. The above indicated secondary structure elements were extracted from the respective crystal structures. See also Fig. 1C and SI Fig. S2.

Fig. S5: NMR data regarding the comparison of the structures of the metal bound rubredoxin-like domain in solution in the isolated form and in the presence of the following kinase domain. The picture shows a superposition of the ^{1}H-^{15}N-HSQC spectra of ^{15}N-D-His-PknG74-420 (RD-KD, black) and ^{15}N-PknG74-147 (RD, red). The RD was always present in the reduced, Zn^{2+} bound state. The assignments for PknG74-147 are indicated by the one-letter amino acid code and the sequence positions (6). The presence of the His-tag at the N-terminus and of the kinase C-terminus of the RD in His-PknG74-420 is expected to result in different chemical shifts for the RD N- and C-terminal regions compared to the tag free isolated RD. Due to the significantly larger size and the fact that His-PknG74-420 is deuterated some backbone resonances may not be visible because they are broadened beyond detection or because the back exchange of undetectable deuterons to detectable protons did not occur equally well for less solvent accessible backbone amides.

Fig. S6: More data regarding the comparison of the structures of the isolated metal bound rubredoxin-like domain in solution and in the crystal structures of PknG fragments containing additionally the kinase domain. **(A)** Ribbon representations of the RD-KD regions of the three crystal structures. The RD region is colored according to the B-factors (red - small B factors to blue - high B factors). Some residues that are dynamic had no coordinates in the respective pdb file of the crystal structure. The kinase domain is represented in yellow. The B-factors were plotted using the software Pymol with a minimum value of 20 (red) and a maximum value of 50 (blue). **(B)** In the amino acid sequence of the rubredoxin-like motif (RD) shown at the top, residues that were used for the determination of the alignment tensor for the back calculation of the RDCs from the crystal structures are highlighted in red. The spatial position of the respective amino acids in the structure of the RD (based on PDB-ID 4Y0X) is indicated in the ribbon representation. Plots of the linear correlation between experimental RDCs (partial alignment with 17 mg/ml phages PF1) and those back calculated

based on the three published crystal structures using the software PALES (10) are shown below and to the right. The data for the Cd^{2+} bound RD of PknG74-750 in complex with the inhibitor AX20017 (PDB-ID 2PZI) (4) are represented as green symbols and those for the Zn^{2+} bound RD of PknG74-405 in complex with an ATP analogue (PDB-ID 4Y12) (5) as red symbols and in complex with ADP (PD-ID 4Y0X) (5) as blue symbols. The bottom two plots compare the back calculated RDCs of the three crystal structures (left: PknG74-405 in complex with ADP or an ATP analogue versus PknG74-750 in complex with an inhibitor, right: PknG74-405 in complex with ADP versus the complex with an ATP analogue). Whereas the structure of the RD in the two nucleotide bound structures is highly similar (right plot), it differs somewhat between the inhibitor bound state of PknG74-750 and the nucleotide bound states of PknG74-405 (left plot).

Fig. S7: More kinase assay data for different PknG constructs and redox conditions. **(A)** & **(C)** SDS-PAGE analysis of the *in vitro* kinase assays using radio labeled ATP and 15% polyacrylamide gels. The gels were analyzed with a phosphorimager. **(A)** shows the gel picture using as kinases His-PknG wild type (wt, blue), His-PknG74-750 (green), or His-PknG74-420 (red) and as substrate His-PknG1-147 with the RD in the oxidized, metal free or reduced, metal bound form. **(B)** Comparison of kinase activities of PknG wild type and of an N-terminal truncated version (PknG74-750) after treatment of their RD metal binding motif with different redox conditions. Kinase activities for the wild type enzyme are represented including the auto phosphorylation in trans of its own N-terminus (see upper band on gel picture in (C)). **(C)** shows the respective SDS PAGE analysis using as kinases His-PknG wild type (wt, blue & red) or His-PknG74-750 (green & black) with the RD either in the reduced, metal bound or oxidized, metal free state and as substrate His-PknG1-147 also with the RD either in the oxidized, metal free or reduced, metal bound form. Please, see also the labeling in each figure. **(D)** NMR monitoring of *in vitro* ^{15}N-His-PknG1-75 (NORS) phosphorylation by His-PknG74-420 (RD-KD) based on the superposition of ^{1}H-^{15}N-HSQC spectra of unphosphorylated ^{15}N-His-PknG1-75 (black), after kinase treatment for 3 h at 298 K (red spectra) and further overnight at 310 K (green). A * indicates a peak that appears newly after phosphorylation. Assigned backbone amide crosspeaks that shifted or showed a change in signal intensity are labeled by the one-letter amino acid code and the sequence position (see also SI Fig. S1) (6). The additional label –sc indicates side chain amide protons.

Fig. S8: More NMR data regarding the effect of oxidization of the two RD C-X-X-C-G motifs on the spectral appearance. **(A)** Superposition of the ^{1}H-^{15}N-HSQC spectra of PknG74-147 (RD) in the reduced, metal bound folded state (black) and the oxidized, unfolded state (red). **(B)** Superposition of the ^{1}H-^{15}N-HSQC spectra of the oxidized, unfolded states of His-PknG1-147 (NORS-RD, black) and PknG74-147 (RD, red). **(C)** Superposition of the ^{1}H-^{15}N-HSQC spectra of the oxidized, unfolded state of His-PknG1-147 (black) and of His-PknG1-147-4C/S mutant (red).

Fig. S9: More NMR data regarding the coordination of different metal ions by the two RD C-X-X-C-G motifs. **(A-C)** Superposition of the ^{1}H-^{15}N-HSQC spectra of ^{15}N-His-PknG1-147 (RD) in the oxidized, unfolded state (black) and reduced, metal bound state (red), the metal ion being either Mn^{2+}, Co^{2+}, or Fe^{3+}, respectively. The reducing agent was always TCEP and the counterion Cl^{-}.

Fig. S10: (A) Last snapshots from six independent 250 ns MD simulations of PknG74-420 with the cysteines of the two C-X-X-C-G motifs of the RD in the reduced state and coordinating Fe^{2+} (Fe^{2+} bound) or in the oxidized state with disulfide bridges between C106 and C109, and C128 and C131 (oxidized). The core RD region (residues ~100-140) is shown in red. Protein atoms within 5 Å of ATP and Mg^{2+} forming the binding cavity are represented in space filling mode in cyan. The ATP binding site is on average more accessible and the RD domain is less folded in the oxidized simulations as compared to the Fe^{2+} bound state. **(B)** Distribution of Loop 2 extension (residue 292-297, shown in cyan in Fig. 5B) calculated form three independent 250 ns MD simulations of the Fe^{2+} bound (in blue) and oxidized (in red) states.

Fig. S11: (A) The volume of the ATP binding cavity, and **(B)** solvent accessible surface area (SASA) of residues interacting with ATP (I87, A92, I157, A158, I165, V179, K181, M232, Y234, G236, M283, I292, D293)(4) in the Fe^{2+} bound (left) and oxidized (right) states.

Fig. S12: Data from 250 ns MD simulations of PknG74-420 with the RD in the reduced metal (Fe^{2+}) bound state or the oxidized, metal free state for the characterization of the influence of RD oxidation on the conformation of the RD as well as the kinase. **(A)** Stick representation of residues surrounding the ATP-Mg^{2+} binding pocket. Only one coordination bond remains stable between Mg^{2+} and E280 during the MD trajectory in the Fe^{2+} bound state

(left). In the oxidized state, Mg^{2+} forms two coordination bound with surrounding residues E280 and D293 (right). **(B)** The distance between Mg^{2+} and D293 as a function of the simulation time for the oxidized and Fe^{2+} bound state. **(C)** The distance between the functionally important residue D276 of the catalytic loop and K278 is larger in the oxidized compared to the Fe^{2+} bound state, which may result in an increased catalytic activity of the former state. In the three independent 250 ns simulations, the D276-K278 ion pair is open (> 4 Å) in 6%, 23%, and 47%, respectively, of the simulation time for the Fe^{2+} bound state, and 4%, 37%, 80%, respectively, of the simulation time in the oxidized state.

Supplementary References

1. Walsh, J. D., Meier, K., Ishima, R., and Gronenborn, A. M. (2010) NMR studies on domain diffusion and alignment in modular GB1 repeats. *Biophys J* **99**, 2636-2646
2. Dames, S. A., Junemann, A., Sass, H. J., Schonichen, A., Stopschinski, B. E., Grzesiek, S., Faix, J., and Geyer, M. (2011) Structure, dynamics, lipid binding, and physiological relevance of the putative GTPase-binding domain of Dictyostelium formin C. *The Journal of biological chemistry* **286**, 36907-36920
3. Sieker, L. C., Stenkamp, R. E., and LeGall, J. (1994) Rubredoxin in crystalline state. *Methods in enzymology* **243**, 203-216
4. Scherr, N., Honnappa, S., Kunz, G., Mueller, P., Jayachandran, R., Winkler, F., Pieters, J., and Steinmetz, M. O. (2007) Structural basis for the specific inhibition of protein kinase G, a virulence factor of Mycobacterium tuberculosis. *Proceedings of the National Academy of Sciences of the United States of America* **104**, 12151-12156
5. Lisa, M. N., Gil, M., Andre-Leroux, G., Barilone, N., Duran, R., Biondi, R. M., and Alzari, P. M. (2015) Molecular Basis of the Activity and the Regulation of the Eukaryotic-like S/T Protein Kinase PknG from Mycobacterium tuberculosis. *Structure* **23**, 1039-1048
6. Wittwer, M., and Dames, S. A. (2016) Chemical shift assignment of the intrinsically disordered N-terminus and the rubredoxin domain in the folded metal bound and unfolded oxidized state of mycobacterial protein kinase G. *Biomol NMR Assign* **10**, 401-406
7. Vuister, G. W., and Bax, A. (1993) Quantitative J correlation: a new approach for measuring homonuclear three-bond J(HNH.alpha.) coupling constants in 15N-enriched proteins. *Journal of the American Chemical Society* **115**, 7772-7777
8. Wishart, D. S., and Sykes, B. D. (1994) The 13C chemical-shift index: a simple method for the identification of protein secondary structure using 13C chemical-shift data. *Journal of biomolecular NMR* **4**, 171-180
9. Shen, Y., and Bax, A. (2010) SPARTA+: a modest improvement in empirical NMR chemical shift prediction by means of an artificial neural network. *Journal of biomolecular NMR* **48**, 13-22
10. Zweckstetter, M. (2008) NMR: prediction of molecular alignment from structure using the PALES software. *Nature protocols* **3**, 679-690

Wittwer et al.
SI Fig. S1

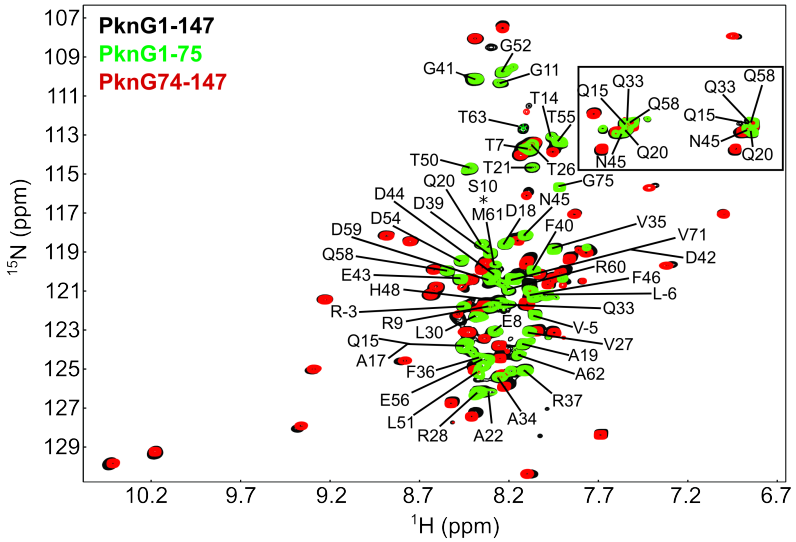

Wittwer et al.
SI Fig. S2

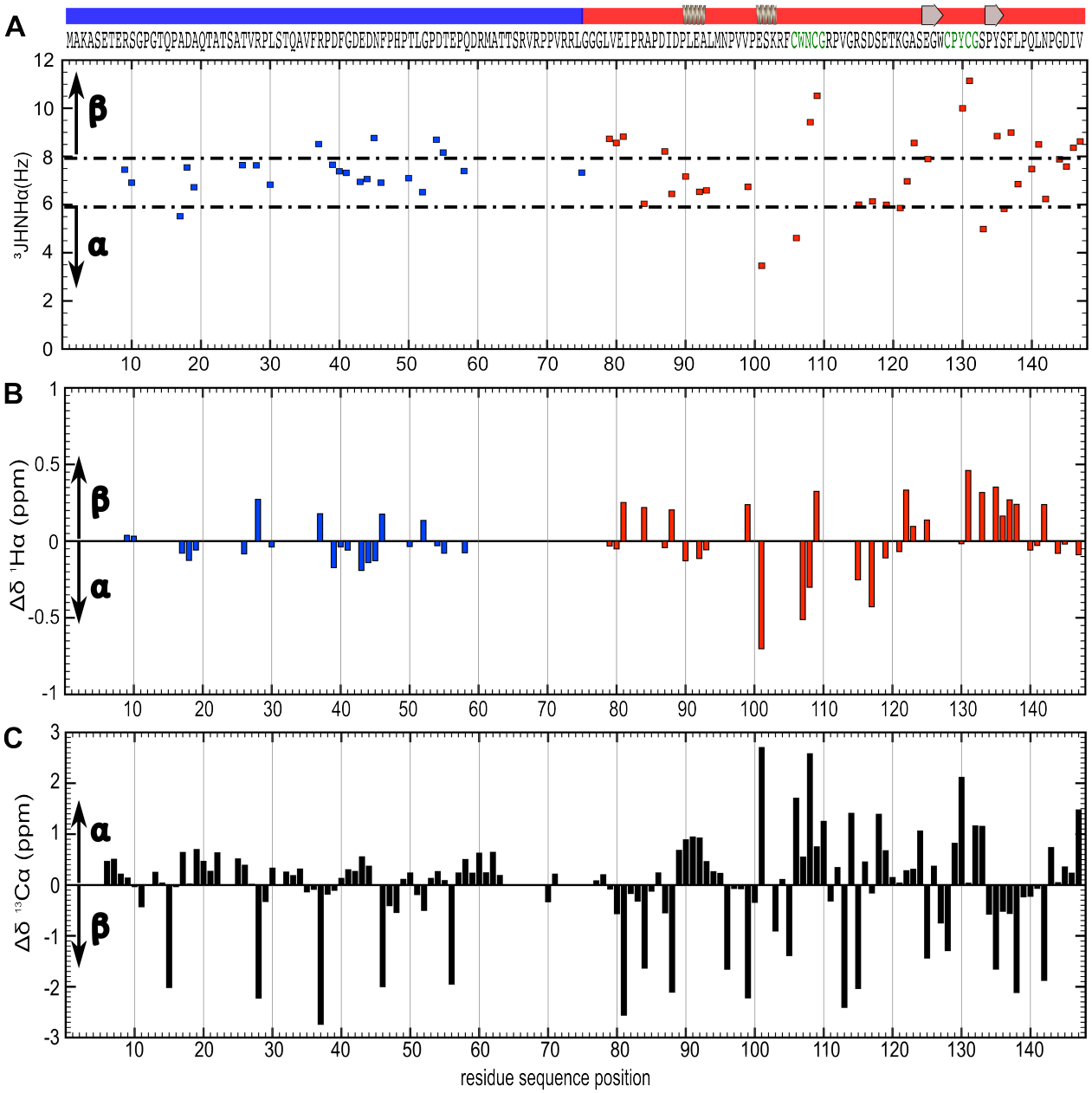

Wittwer et al.
SI Fig. S3

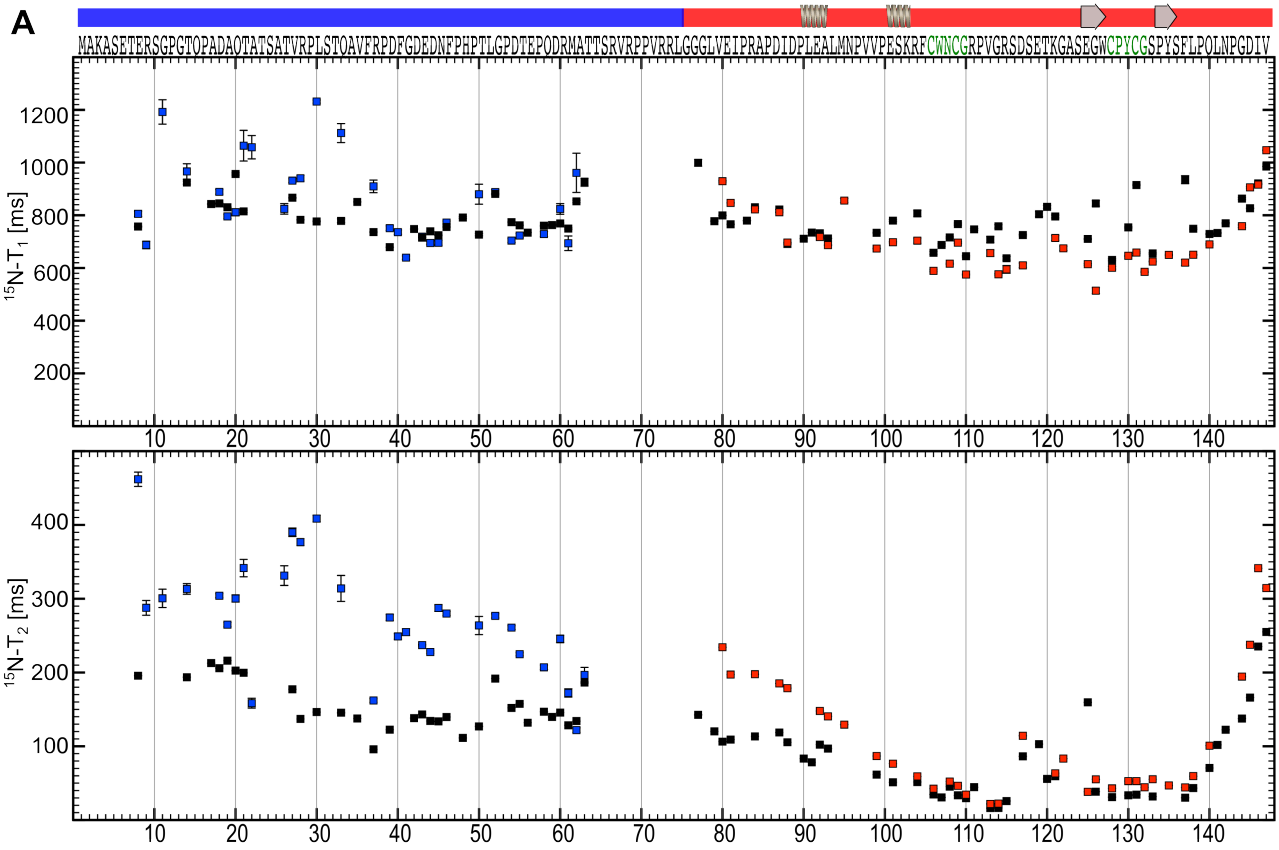

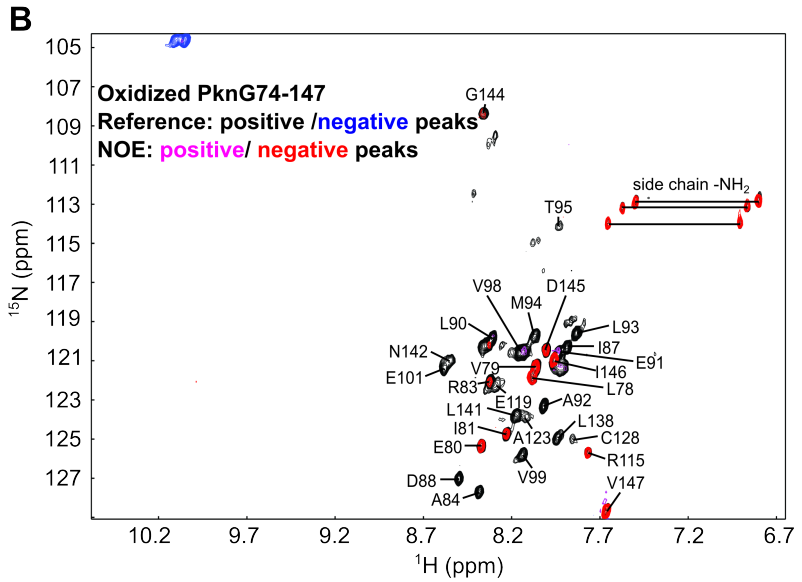

Wittwer et al.
SI Fig. S4

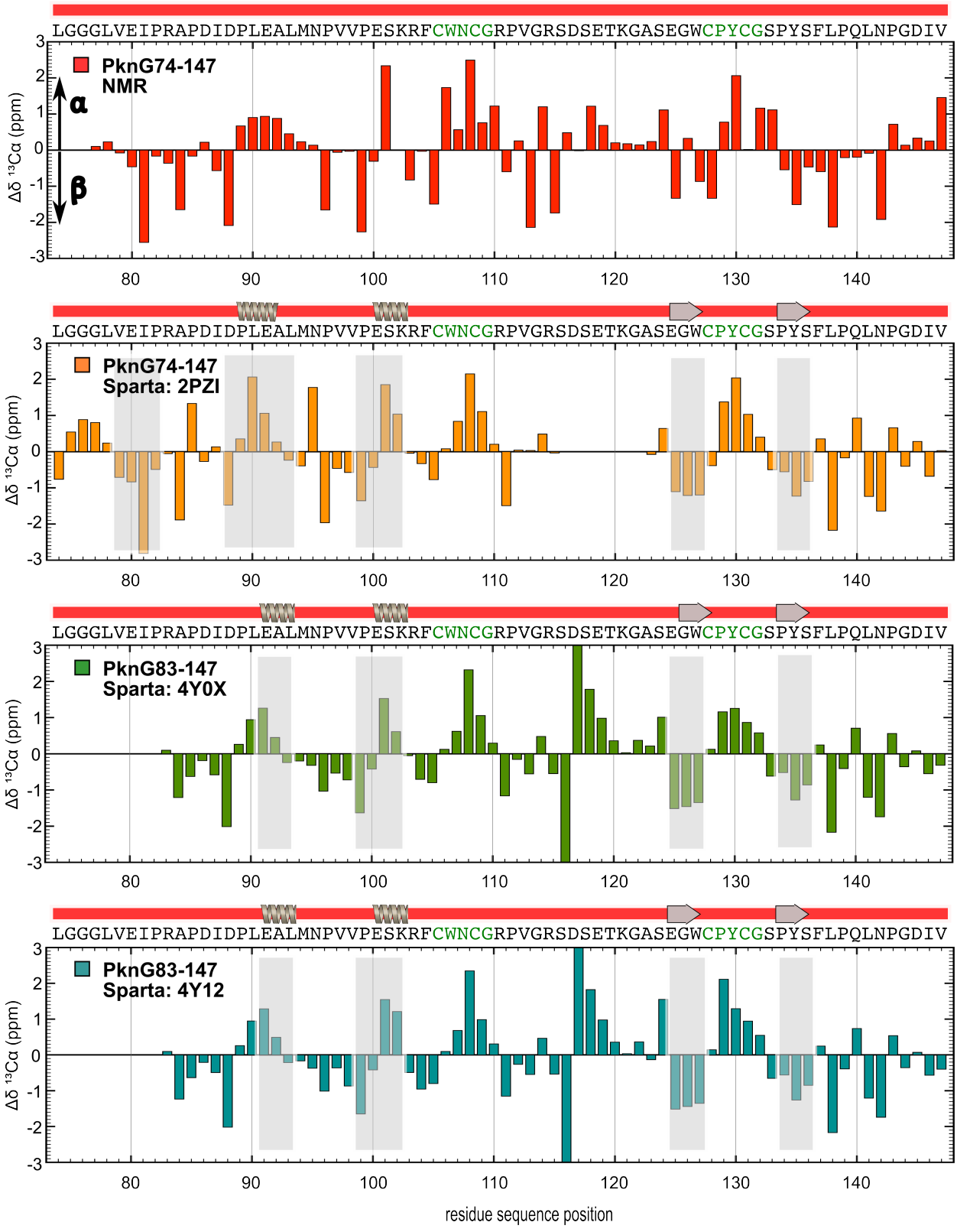

Wittwer et al.
SI Fig. S5

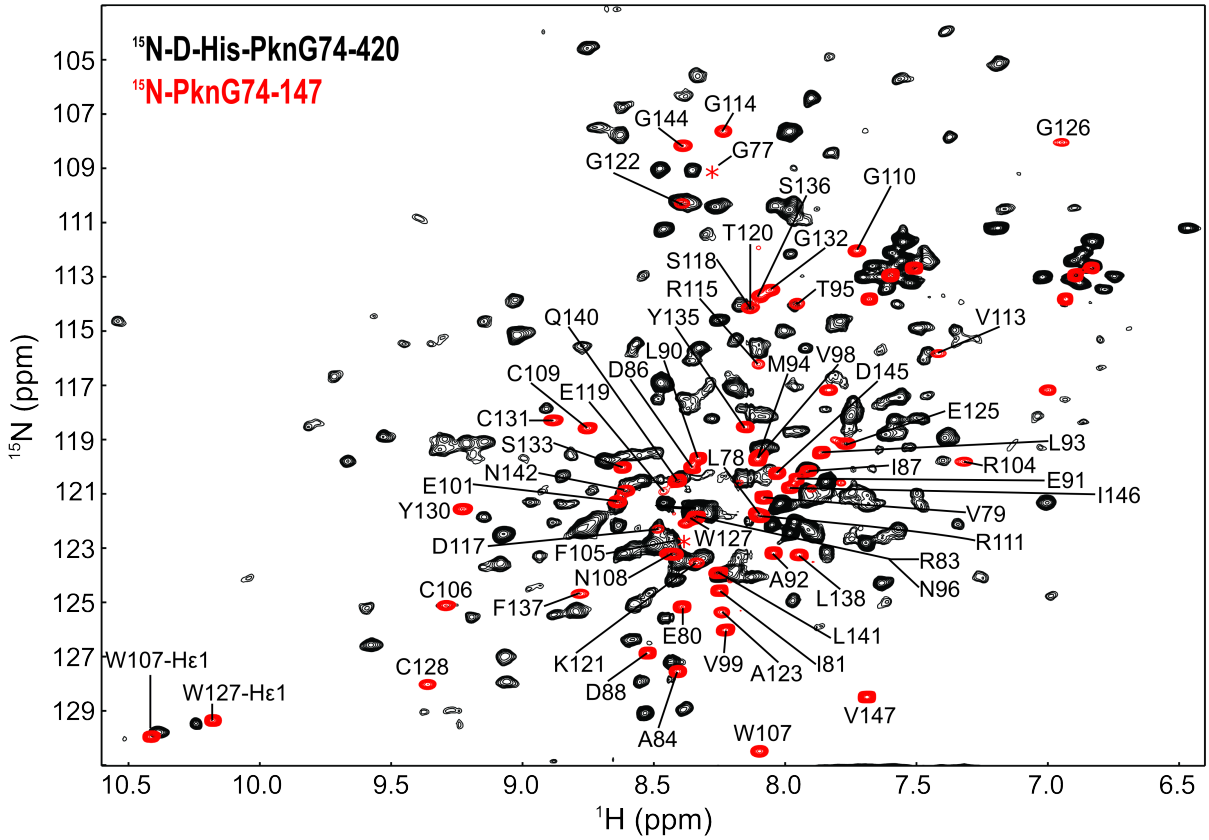

Wittwer et al.
SI Fig. S6

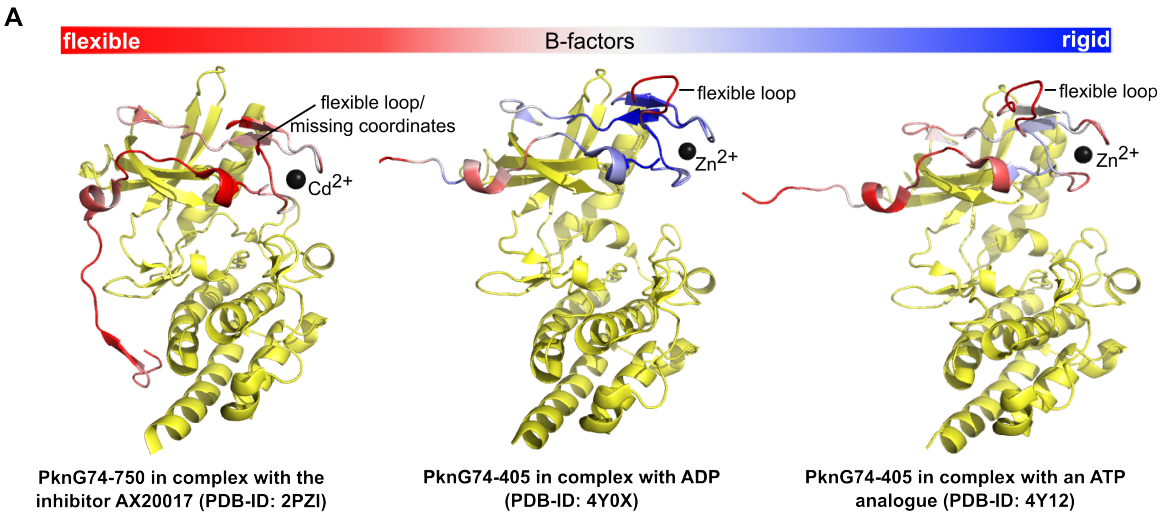

B

flexible loop

N-LGGGLVEIPRAPDIDPLEALMTNPVVPESKRFCWNCGRPVGRSDSETKGASEGWCPYCGSPYSFLPQLNPGDIV-C

80 90 100 110 120 130 140

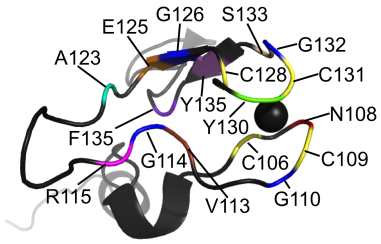

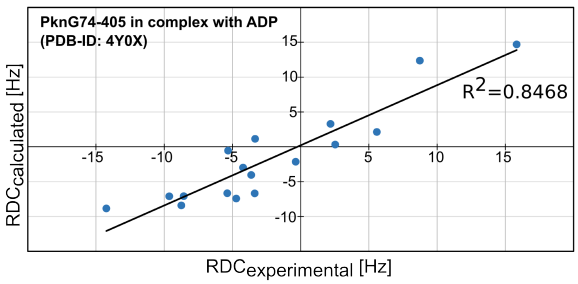

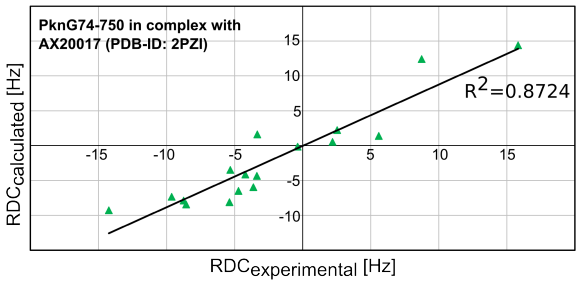

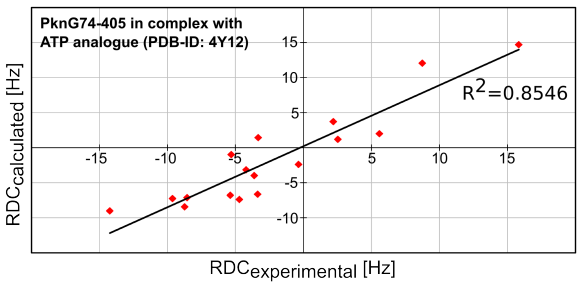

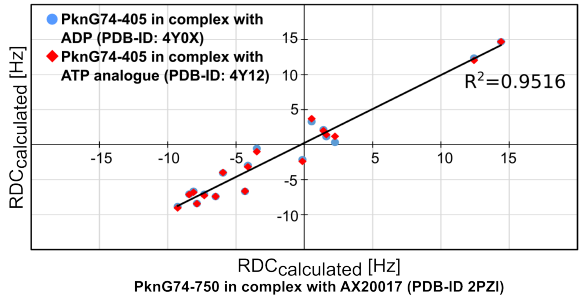

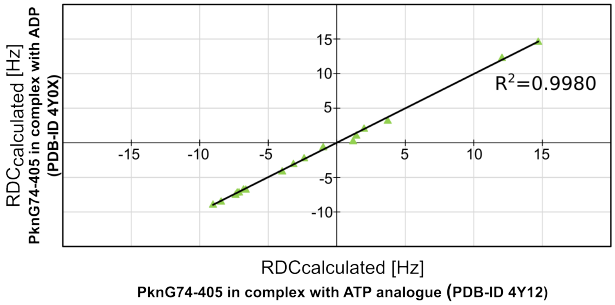

Wittwer et al.
SI Fig. S7

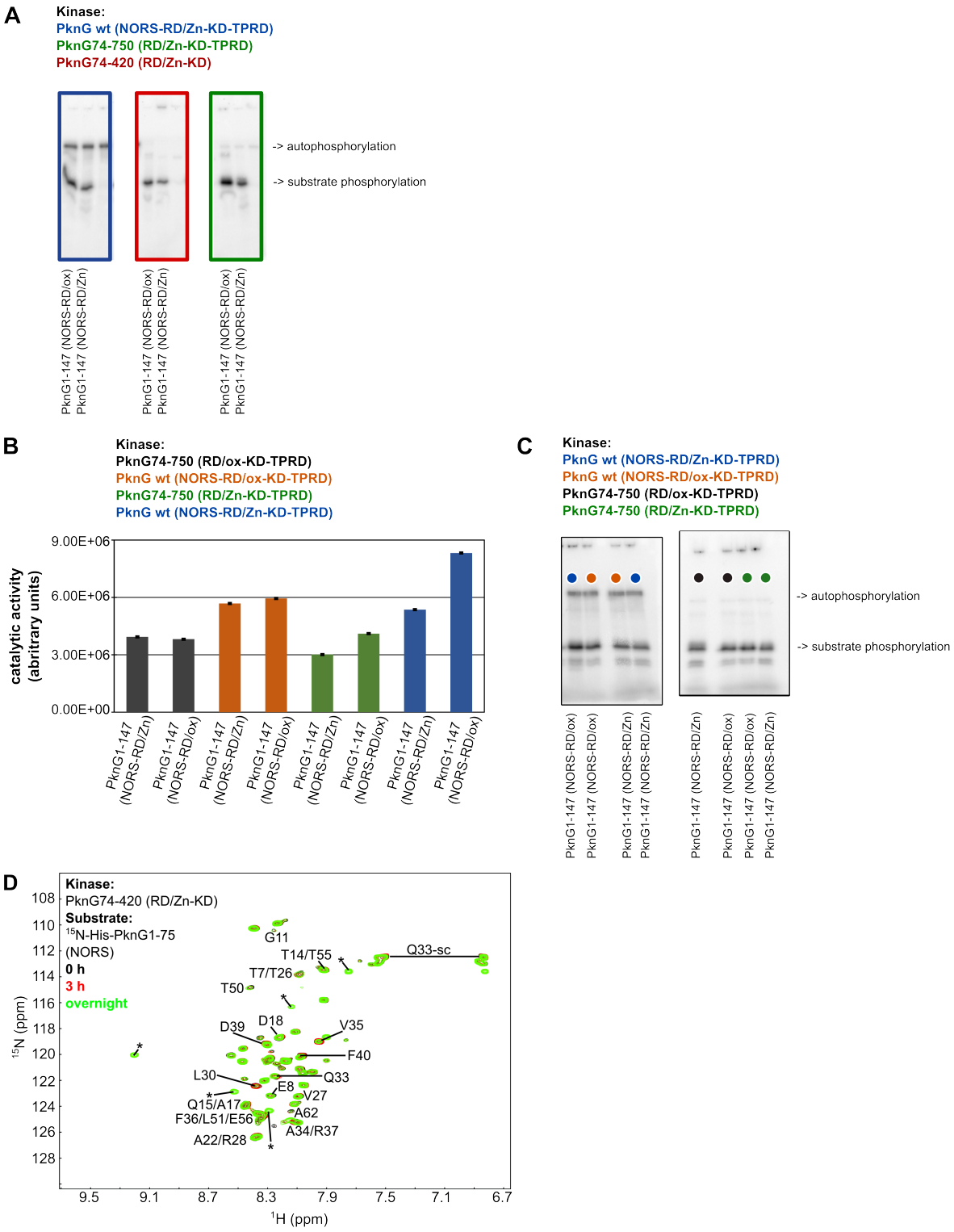

Wittwer et al.
SI Fig. S8

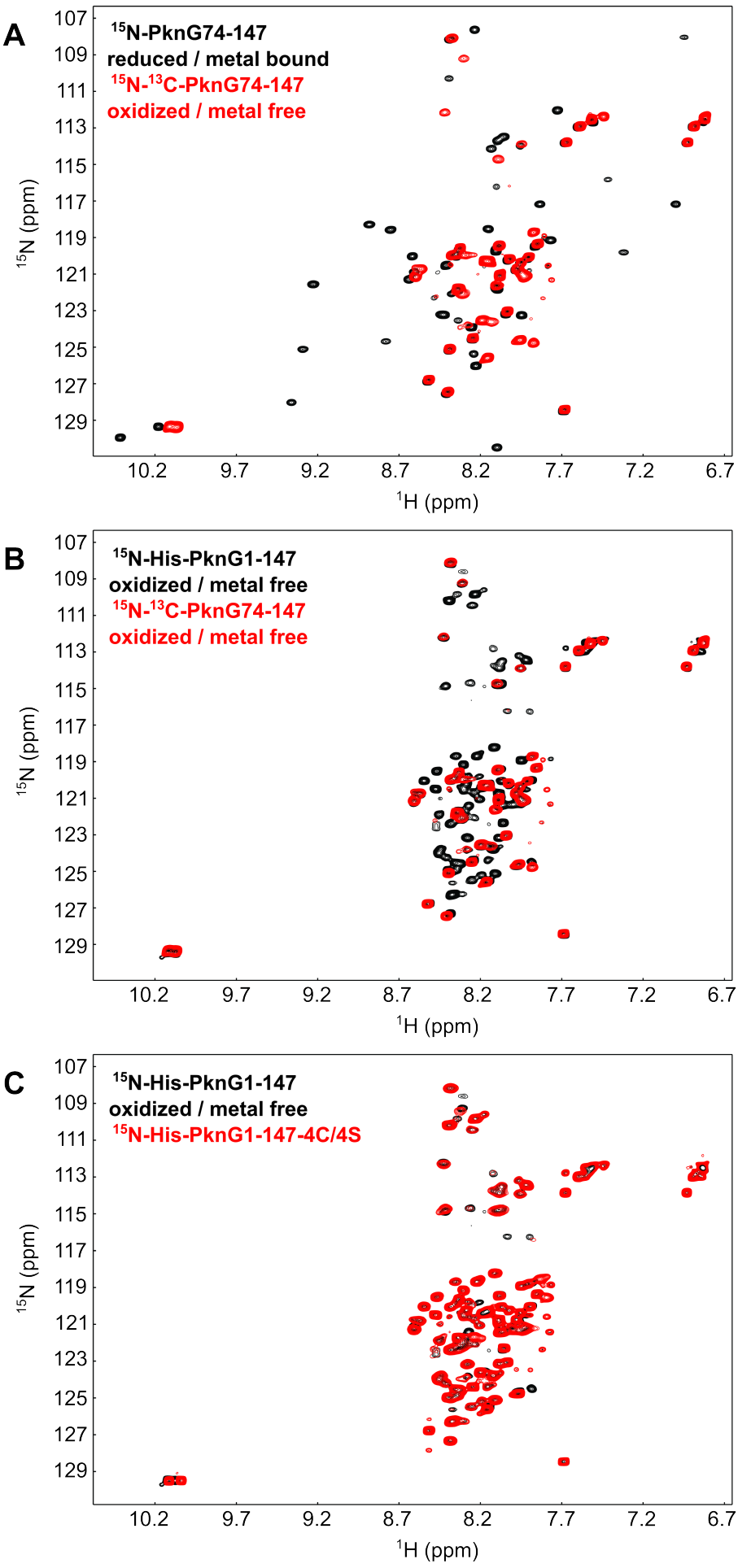

Wittwer et al.
SI Fig. S9

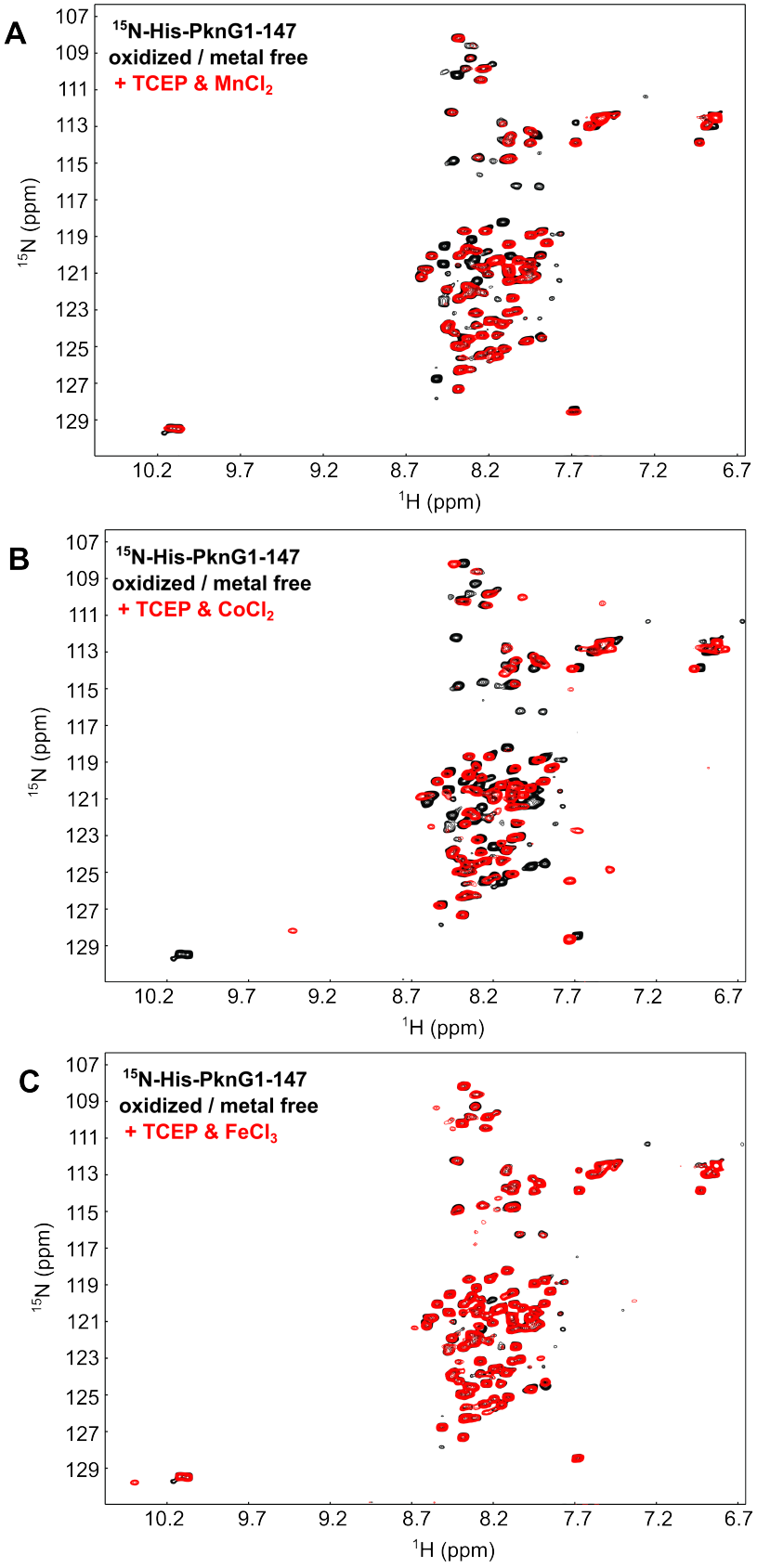

Wittwer et al.
SI Fig. S10

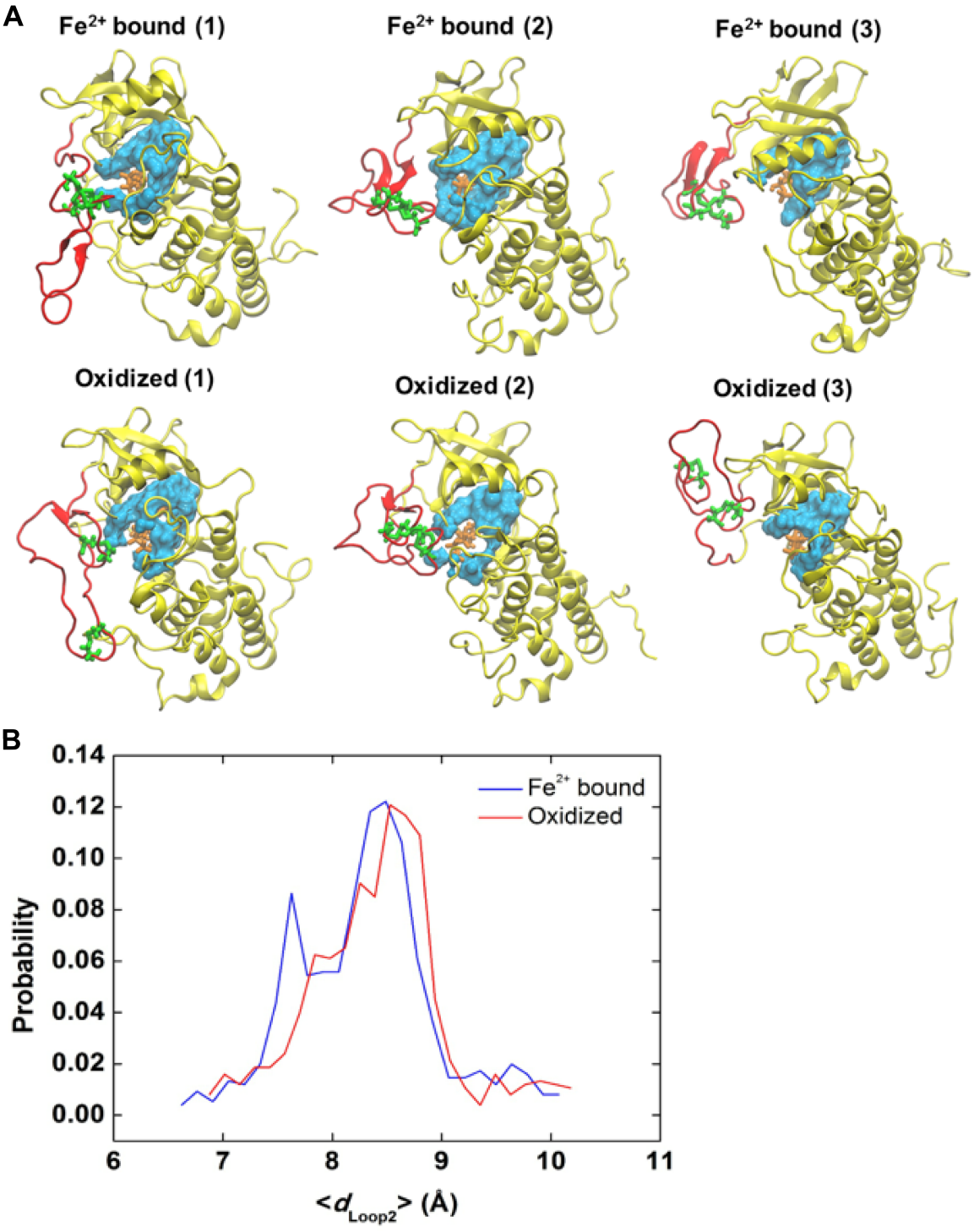

Wittwer et al.
SI Fig. S11

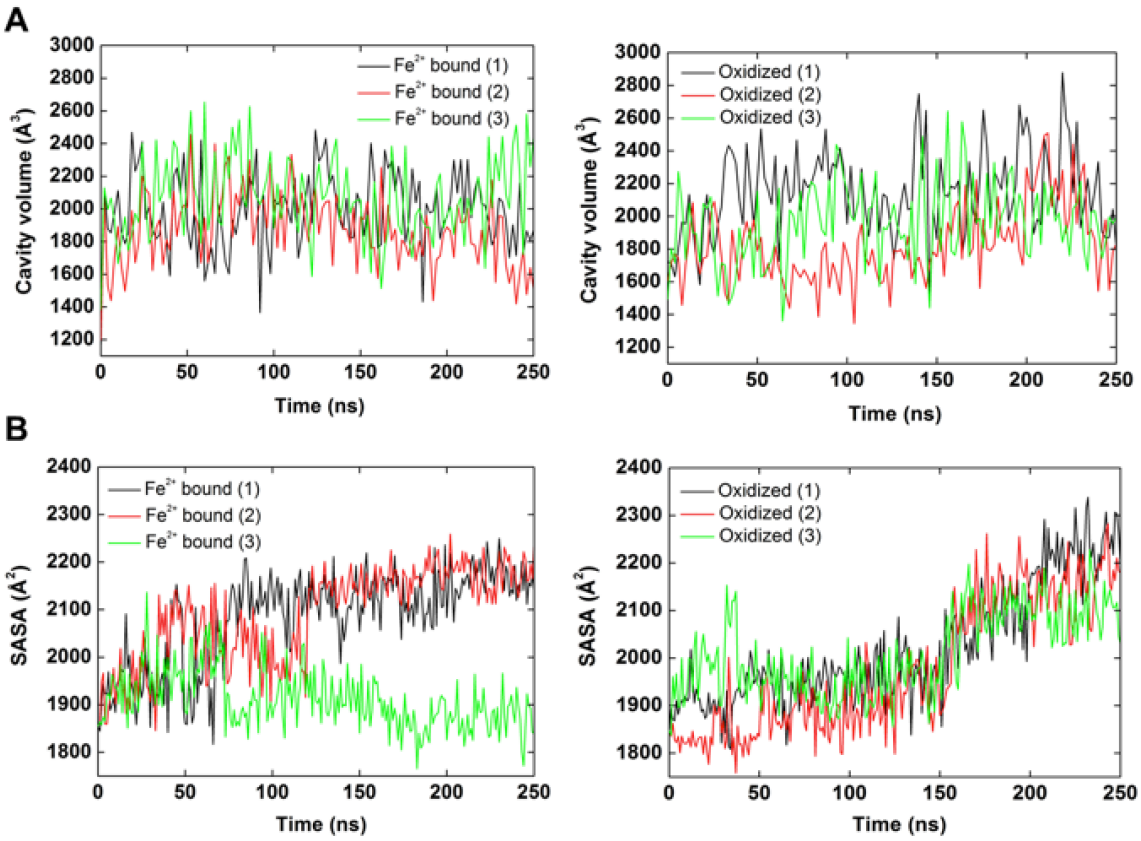

Wittwer et al.
SI Fig. S12

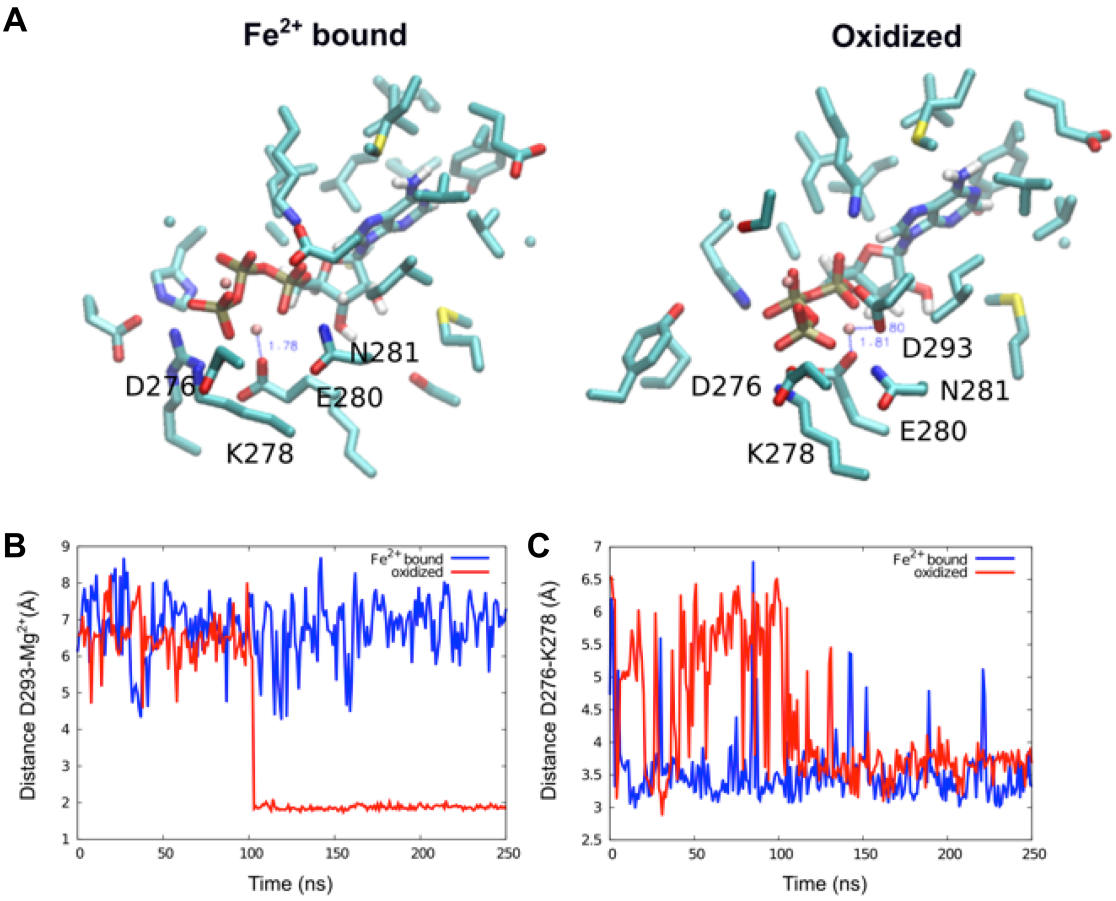

Oxidative Unfolding of the Rubredoxin Domain and the Natively Disordered N-terminal Region Regulate the Catalytic Activity of M. tuberculosis Protein Kinase G

Matthias Wittwer, Qi Luo, Ville R. I. Kaila and Sonja A. Dames

J. Biol. Chem. published online November 3, 2016
